UC Riverside
UC Riverside Electronic Theses and Dissertations

Title
Rapid and Facile Growth of High-Quality 2D $MoTe_2$

Permalink
https://escholarship.org/uc/item/7gg961p4

Author
Yadav, Prachi Rajendra

Publication Date
2024

Peer reviewed|Thesis/dissertation

eScholarship.org Powered by the California Digital Library
University of California

UNIVERSITY OF CALIFORNIA
RIVERSIDE

Rapid and Facile Growth of High-Quality 2D MoTe2

A Dissertation submitted in partial satisfaction
of the requirements for the degree of

Doctor of Philosophy

in

Materials Science and Engineering

by

Prachi Yadav

June 2024

Dissertation Committee:
Dr. Ludwig Bartels, Chairperson
Dr. Juchen Guo
Dr. Mahesh Neupane

Copyright by
Prachi Yadav
2024

The Dissertation of Prachi Yadav is approved:

____

____

____

Committee Chairperson

University of California, Riverside

Acknowledgments

In these seemingly small words, I express my heartfelt gratitude to all my family, friends, and mentors for truly seeing me when I needed it most. It's challenging, if not impossible, for others to fully grasp the depth of one's passion or dreams, yet these individuals have somehow woven my purpose into their own lives over the past several years. I extend my sincere thanks to each of you. During the most trying times, your kindness, support, generosity, patience, and love have sustained me beyond measure.

This thesis represents my endeavor to understand science and contribute to pushing the frontiers of technology, made possible by your unwavering support.

I dedicate this work to the somewhat uncertain, somewhat timid, yet inherently brave girl who yearns to explore beyond her comfort zone, driven by curiosity to see where it may lead (and might be reading this at the moment).

ABSTRACT OF THE DISSERTATION

Rapid and Facile Growth of High-Quality 2D $MoTe_2$

by

Prachi Yadav

Doctor of Philosophy, Graduate Program in Materials Science and Engineering
University of California, Riverside, June 2024
Dr. Ludwig Bartels, Chairperson

Transition metal dichalcogenides based on transition metals (like Mo, W, Ta) and chalcogens (like S, Se, Te) are important two-dimensional (2D) materials in materials research for a range of applications including but not limited to electronics, photonics, optoelectronics, sensing, and photovoltaics. At the scale of the dimensions of these materials, the properties differ from their properties at larger dimensions. To exploit these interesting properties for novel applications, the growth methods of the materials are an important aspect. While materials research has advanced over several decades in this area, substantial challenges exist in their controlled and rapid growth. $MoTe_2$ is an especially challenging material to grow among the TMD materials and needs more investigation given its superior properties.

In this thesis, I report the study of the parameters of growth mechanisms of materials like $MoTe_2$, $MoSe_2$, and MoS_2 on SiO_2, Si, and GaN substrates. I present reproducible growth of $MoTe_2$ in an ultra-high vacuum (UHV) environment using co-deposition of transition metal and chalcogen. The phase diagram developed for this system shows that both semimetallic and semiconducting phases of $MoTe_2$ can be grown on SiO_2 substrates. With

the addition of a MoS_2 underlayer, the phase of $MoTe_2$ is affected significantly. A similar growth mechanism can be used to grow $MoSe_2$.

The quality of the materials is investigated using Raman spectroscopy, photoluminescence spectroscopy, cross-sectional transmission electron microscopy, scanning electron microscopy, low energy electron diffraction, X-ray photospectroscopy, energy dispersive spectroscopy, and electrical characteristics.

Table of Contents

Chapter 1: Background ... 1

1.1. A brief history of 2D materials in semiconductor processing ... 1

1.2 Transition Metal Dichalcogenides (TMDs) ... 4

1.3 TMDs structure ... 5

1.4 TMD phases... 6

Chapter 2: Materials in this study ... 13

2.1. MoS ... 13

2.2. $MoTe_2$ ... 16

2.3. Bandgap Brillouin zone, and lattices ... 18

2.4. Phase transition ... 24

Chapter 3: Growth and characterization methods ... 26

3.1. Growth methods ... 26

3.2. Characterization techniques ... 37

Chapter 4: UHV chamber and two-step growth of $MoTe_2$ ... 51

4.1. Growth chamber ... 51

4.2. Substrate preparation……………………......……………………………58

4.3. Two-step growth of MoS_2………...58

4.4. MoS_2 growth………..67

Chapter 5: Single step TMD growth 70

5.1.Motivation.. **70**

5.2. Experiments……………………......…………………………………73

5.3. Characterization ………..75

5.4. Results………..…...78

5.4. Summary………..…...80

Chapter 6: Implications, Outcomes, and Summary 81

References 85

List of Publications

Yang, H. I.; Ning,Y.; Jin,J.; Juarez, M.; Henshaw, J.; Azizur-Rahman, K.; Flores, B.; Meneses, N.; **Yadav, P. R.;** Villarreal, S; Hill, M. E.; Sorger, V.; Mounce, A.; and Bartels, L., Photoluminescent Substrate-Scale 3R WS_2/MoS_2 Heterostacks on GaN. (in review)

Yang, H. I.; Coyle, D. J.; Wurch, M.; **Yadav, P. R.;** Valentin, M. D.; Neupane, M. R.; Almeida, K.; Bartels, L., Epitaxial Molybdenum Disulfide/Gallium Nitride Junctions: Low-Knee-Voltage Schottky-Diode Behavior at Optimized Interfaces. ACS Applied Materials & Interfaces **2021**, 13 (29), 35105–35112.

List of Figures

Chapter 1:

Figure 1.1. Periodic table showing the transition meal and chalcogens that make the layered TMDs…………………………………………………………..….. 4
Figure 1.2. TMDs : (top) TMD layered structure with transition metal cation and chalcogen anion; (bottom) coordination-dependent geometry of the molecular structure. …....8
Figure 1.3. TMD structures: (a) top view of layered TMDs; (b) side view of layered TMDs..…10

Chapter 2:

Figure 2.1. Molecular orbital energy-level diagram of 2H-MoS_2………………………14
Figure 2.2. d orbitals splitting in transition metal atoms with respect to the coordination and the related Fermi energy level……………..……………………………15
Figure 2.3. (a) 1T' $MoTe_2$ monolayer crystal structure and the related crystal symmetries. (b) Bulk monoclinic 1T' $MoTe_2$ and the related crystal symmetries. (c) Bulk orthorhombic 1T' $MoTe_2$ and the related crystal symmetries. Bulk hexagonal $MoTe_2$ and the related crystal symmetries…………………………………16
Figure 2.4. (top) and Brillouin zone of 2H MoS_2; energy band structure of 2H MoS_2 (bottom-left) bulk; (bottom-right) monolayer. The red arrows show the indirect bandgap between conduction band minima and valence band maxima…22

Chapter 3:

Figure 3.1. (a) CVD growth system; (b) Sputtered growth system; (c) MBE growth system……………………………………………………………………..33
Figure 3.2. Electron relaxation mechanisms- Raleigh scattering, anti-Stokes scattering, and Stokes scattering………………………………………………………37
Figure 3.3. Simplified representation of Raman instrumentation……………….……..38
Figure 3.4. Raman vibration modes of TMDs: (a-b) TMD structures; (c) in-plane and out-of-plane modes…………………………………………………….…….38
Figure 3.5. Simplified sketch of XPS instrumentation……………………………..…...43
Figure 3.6. Simplified TEM sketch and electron interactions with matter…………..…45
Figure 3.7. Simplified sketch of LEED instrumentation………………………………49
Figure 3.8. Four probes sensing on a sample……………………………………….....50

Chapter 4:

Figure 4.1. Transition metal e-beam evaporators and chalcogen Knudsen cells in growth chamber SolidWorks drawing. …………………………………………53
Figure 4.2. Heater assembly photo (a) side view and (b) top view; (c) SolidWorks drawing of the heater assembly and the wire routing aluminum block…...54
Figure 4.3. Quartz crystal with gold electrodes on top and bottom; (b) QCM monitoring for evaporation rate of atoms…………………………………………...57
Figure 4.4. A timeline of $MoTe_2$ growth using the two-step method…………………59
Figure 4.5. Sample A1, B1, and C1 represent the Raman spectra of $MoTe_2$ growth on SiO_2/Si substrates. Sample A2, B2, and C2 represent the Raman spectra of $MoTe_2$ growth on MoS_2/SiO_2/Si substrates. Sample A3, B3, and C3 represent the Raman spectra of $MoTe_2$ growth on MoS_2/GaN/Si substrates………..60
Figure 4.6. Four devices are fabricated on different areas of the sample to test the uniformity of film quality…………………………...…………………62
Figure 4.7. (a) 4 probe measurement setup. (b) Measurement stack and pads used to measure the electrical characteristics…………………………..……..…..62
Figure 4.8. IV characteristics of 2H $MoTe_2$ on SiO_2/Si……………………….……..…….63
Figure 4.9. XPS of $MoTe_2$ on SiO_2/Si……………………….………………...………63
Figure 4.10. SolidWorks drawing of QCM and evaporators in the chamber…………….65
Figure 4.11. SolidWorks drawing of MoS_2 growth section of the chamber……………...65
Figure 4.12. MoS_2 growth……………………………………………………………...66
Figure 4.13. Raman and PL spectrum of MoS_2 on SiO_2/Si……………………………68
Figure 4.14. UHV growth chamber (a) top view photo; (b) front view photo; (c) side view SolidWorks drawing…………………………………………...……69
Figure 4.15. A timeline of single-step growth of $MoTe_2$……………………………….…...69

Chapter 5:

Figure 5.1. Manipulator arm (a) top view, (b) side view, and (c) front view…………….71
Figure 5.2. Chamber setup with $MoTe_2$ (left) and MoS_2 (right) growth regions. The substrate is placed on a heater arm that moves the sample between two growth regions. (b), (c) Optical images of multilayer $MoTe_2$ and monolayer MoS_2 growth on SiO_2/Si respectively. (d), (e) Raman and photoluminescence spectrum of MoS_2 underlayer grown on SiO_2/Si respectively. ……………..…74
Figure 5.3. Raman spectrum of 2H $MoTe_2$ grown on SiO_2 substrate; (b) Ramana spectrum of 2H $MoTe_2$ grown on SiO_2 substrate with underlying MoS_2 layer; (c) SEM images of planar films; (d) Raman spectrum of 1T' $MoTe_2$ grown on SiO_2 substrate. ……………………………………………………………….…76

Figure 5.4. TEM image of layered $MoTe_2$ grown on $MoS_2/SiO_2/Si$ substrate. (b) Zoomed-in region of the TEM image shows atomic arrangements in the layered structure. (c) EDS mapping of a section of the TEM lamina. ………..…...…77
Figure 5.5. Phase diagram of Mo-Te growth via co-deposition method. The green color represents 2H phase of $MoTe_2$ and the red color represents the 1T' phase of $MoTe_2$. …………………………..……………………………………………79

Chapter 6:

Figure 6.1. Raman spectrum of $MoSe_2$ grown on SiO_2/Si…………………………………81
Figure 6.2. Raman spectrum of heterostructure: $MoS_2/MoTe_2/MoS_2/SiO_2/Si$…………...82
Figure 6.3. LEED image of $MoTe_2/MoS_2/GaN$. …………………………………….……...83
Figure 6.4. Cross-sectional TEM image and (b) TEM Fourier transform of the $MoTe_2/MoS_2/GaN$……………………………………………………….……..84

Chapter.1. Background

1.1. A brief history of 2D materials in semiconductor processing

Moore's Law, a prediction made by Gordon Moore, co-founder of Intel, in 1965 states that the number of transistors on a microchip would double approximately every two years. This doubling of transistors leads to a rapid increase in computing power and a decrease in the cost per transistor. The prediction became a guiding principle for the semiconductor industry, driving technological advancements.

While Moore's Law has held for several decades, there are debates about its sustainability as we approach the physical limits of semiconductor miniaturization.[1,2] The physical limits to how small transistors could become rely on fabrication tools and quantum effects and issues related to heat dissipation at this scale. Considering this, innovations like new materials, architectures, and technologies continue to push the boundaries of computing power. Truly going beyond Moore’s law would also open an exciting arena for the hardware that can complement the startling rise of the artificial intelligence (AI) market. The semiconductor industry is exploring various avenues to achieve this. Some potential directions include:

1. Advanced Materials: Advancing semiconductor technology involves researching novel materials like 2D materials and nanotubes to build more potent and energy-efficient transistors.[3–5]
2. Quantum Computing: Quantum computing utilizes quantum mechanics principles to achieve computation speeds beyond classical computers, offering solutions to complex problems.[6,7]

3. Neuromorphic Computing: Neuromorphic computing, inspired by the human brain, aims to replicate biological neural networks for enhanced efficiency and pattern recognition in computer systems.[8–10]
4. Parallel Processing and Specialized Chips: Rather than relying solely on increasing the number of transistors on a single chip, there is a focus on developing specialized chips for specific tasks and improving parallel processing capabilities to enhance overall computing power.[11]
5. 3D Stacking: this innovative approach involves assembling multiple transistor layers in a three-dimensional configuration for increased computing power and density, moving beyond reliance on 2D miniaturization.[12]

The industry is likely to see a combination of these technologies to meet the growing demand for more powerful and efficient computing solutions. Various types of materials are crucial for these advancements in improving semiconductor technology. Some key material categories include: 2D materials in thin film form;[13] nanomaterials like nanotubes, nanowires, nanoribbons;[14–17] quantum dots;[18,19] III-V semiconductors like GaAs, InP;[20] topological insulators exhibiting unique properties at the surface compared to bulk;[21] ferroelectric materials;[22] high dielectric materials;[23,24] organic semiconductors and more.[12,25]

2D materials, like graphene and transition metal dichalcogenides (TMDs), are favored for their atomic-scale thickness, driving the trend toward miniaturization in electronic devices. This thin profile not only reduces the size of electronics but also boosts performance due to the unique properties at this scale, enabling faster and more energy-efficient operation. Also, beyond electronics, 2D materials showcase versatility-exceptional strength, surface sensitivity, and tunable optical characteristics.[26] They find applications in diverse fields, from medical devices to chemical processes, making them a focal point for impactful research and innovation.[27] Several 2D materials have garnered attention in the field of materials science and semiconductor research. Some of the notable ones include: graphene;[15,26,28,29] TMDs;[30,31] hexagonal boron nitride (h-BN);[32–34] phosphorene and black phosphorus;[35–37] silicene.[38,39]

For the fabrication of electronic components, a range of materials with different properties is required, including semiconductors, metals, insulators, and high-k dielectrics, to construct sophisticated electronic chips tailored for specific applications.[40] The 2D materials become viable candidates for these roles based on their electronic properties, growth mechanisms, integration into devices, compatibility, and applications.[41,42]

In terms of the versatility of these materials, transition metal dichalcogenides pique the research interest. A typical TMD structure is composed of a transition metal atom sandwiched by covalent bonding between two chalcogen atoms and adjacent TMD layers stacked with van der Waals (vdW) interactions between them. By the virtue of combination of the stacking sequence of layers, the transition metal, the chalcogen element, and defects we get a wide range of these materials with unique properties.[30,41,43–45]

1.2. Transition Metal Dichalcogenides (TMDs)

A little over a century ago, in 1923, Roscoe Dickinson and Linus Pauling published their study on the crystal structure of molybdenite based on X-ray photography and Laue photography characterization.[46] The lattice parameters they found led to the identification of the two MoS_2 structures with one Mo atom between two S atoms in a hexagonal system. Most of the samples in the earlier reports were prepared by the chisel method to obtain as fine structures for metrology as possible. Frindt in their 1965 work seems to be the pioneer in using adhesive tape to obtain thin MoS_2 crystal films by exfoliation.[47] This led to Wilson and Yoffe's investigation of nearly 40 layered TMD structures and their characterization using X-ray diffraction (XRD), Transmission Electron Microscopy (TEM), Scanning Electron Microscopy (SEM), Energy Dispersive Spectroscopy (EDS), and optical absorption in 1969.[48] These historical advancements paved the path to the eventual evolution of 2D TMD materials research for cutting-edge electronics and other applications.

Figure 1.1. Periodic table showing the transition meal and chalcogens that make the layered TMDs.[49]

1.3. TMDs structures

The transition metals (elements from groups 3 to 12) and the chalcogens (elements from group 16 of the periodic table) make the TMD molecular structures. The covalently bonded transition metal atom with two chalcogen atoms can be represented as $MX_2$where "M" is the transition metal atom between two chalcogen atoms represented by "X". As such, within one layer, the atoms are covalently bonded. Each layer of covalently bonded X-M-X atoms in the MX_2 molecules is bonded to adjacent layers along the c-axis via the vdW interactions. By virtue of the sequence of alignment of the layers in multilayer structures, TMDs can occur in various polymorphs. The polymorph phases are discussed further in the upcoming section. The inter- and intra-layer correlations can be explained with hybridized orbitals and they govern the properties of the TMD structure.[50,51] In a TMD molecule, the metal atom has an oxidation state of +4 due to the outermost s and d electrons and the chalcogen atom has an oxidation state of -2. The other d electrons in the transition metal atom are important in contributing to the characteristic properties of their compounds as well. Some of them are enlisted here: magnetic properties due to the number of unpaired/paired electrons, color due to the d-d electron transition, geometric structures due to co-ordination complexes, optical properties due to charge transfer and crystal field splitting, electronic properties based on quantum mechanical effects, and more.[44,48,51–55]

In this thesis, our attention will be directed toward a select subset of TMDs from the vast array available. The transition metals (Mo, Ta, W) are elements from periods 5, and 6 and groups 5 and 6. The chalcogens (S, Se, Te) are from periods 3, 4, and 5 and group 16.

Element	Electron configuration	Oxidation states; (Valence electrons)
Mo_{42}	[Kr] $4d^5$ $5s^1$	+2, +3, +4, +5, +6; (6 electrons)
Ta_{73}	[Xe] $6s^2$ $4f^{14}$ $5d^3$	+3, +4, +5; (5 electrons)
W_{74}	[Xe] $6s^2$ $4f^{14}$ $5d^4$	+2, +3, +4; (6 electrons)
S_{16}	[Ne] $3s^2$ $3p^4$	-2, +2, +4, +6; (6 electrons)
Se_{34}	[Ar] $4s^2$ $3d^{10}$ $4p^4$	-2, +4, +6; (6 electrons)
Te_{52}	[Kr] $5s^2$ $4d^{10}$ $5p^4$	-2, +2, +4, +6; (6 electrons)

Table 1.1. Electron configuration and oxidation states of transition metals

1.4. TMD Phases

The polymorphs or "many" (from ancient Greek word- "poly") "forms" or "shapes" (from ancient Greek word- "morphs") of TMDs are represented with a combination of integer numbers and alphabets. The numbers denote the count of layers in repeating sequence and the letters denote the crystal system assumed by the stacking polytype. T is the tetragonal crystal system, H is the hexagonal crystal system and R is the rhombohedral crystal system. In stacking, the polytypes can undergo distortion leading to the breaking of the interlayer crystal symmetry.[41,45,48,53,56,57]

In the layered arrangements of MX2, let us assume that the capital letters (like A, B, and C) denote the chalcogen (X) atoms and the small case letters (a, b, and c) represent the metal (M) atoms. As represented in table 1.2., the predominant coordination geometries are either octahedral or trigonal prismatic. When looking at TMDs as layered structures, it is important to take into account the coordination of the neighboring atoms. Within a layer of such 2D materials, the partial ionic nature in the bonds of X-M-X and adjacent molecules and the attractive-repulsive forces result in a specific geometry. When the M-X bond is more ionic, the distance between the X ions is larger, due to electrostatic repulsion, resulting in octahedral coordination. Conversely, when the M-X bond is more covalent, the resulting geometry is trigonal prismatic due to the preferred directionality of the covalent bond and stronger overlap of the M and X wavefunction overlap.[58,59]

The vdW interactions between the subsequent layers define the phase of the multilayered structures. The MX_2type of TMDs have a 6:3 chalcogen to metal coordination in the layers. With the chalcogen hexagons stacked on top of one another and the metal occupying the trigonal prismatic hole, the 2H phase acquires a trigonal prismatic structure with AbA BaB type of layer stacking.

The chalcogen atoms are stacked directly on top of one another in each layer and therefore noted as "A" and "A" or "B" and "B" or "C" and "C". The metal atom placement is slightly staggered with respect to one another and therefore noted as "b" and "a" in adjacent layers.

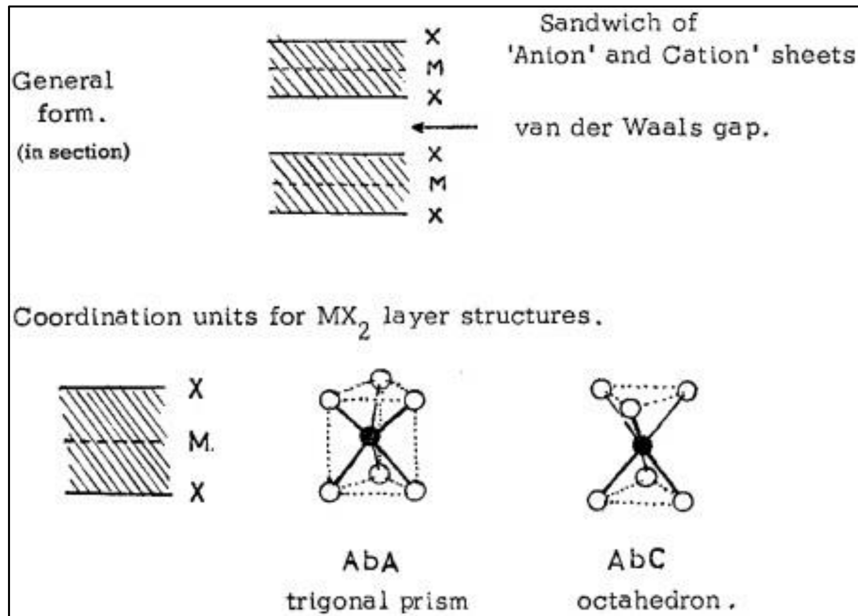

Figure 1.2. TMDs: (top) TMD layered structure with transition metal cation and chalcogen anion; (bottom) coordination-dependent geometry of the molecular structure.[48]

In the case of the 3R phase, we find three possible sites with the metal atoms in the three adjacent layers staggered with respect to each other in a rectangular primitive cell.[45] The 1T phase has chalcogen and metals in three sites of the cell repeating similarly in each layer making the AbC AbC type of stacking. These materials can transform one phase to another. Such transformations will be discussed in detail in future sections. But fundamentally, the modes of the transformations occur via shear, gliding, and atomic displacement under varying ambient conditions.[48,53,60] The transformations can lead to modified or distorted forms of the previously discussed 2H or 1T structures.

To understand the different properties of these materials with regard to the phases, the significance of these structures is discussed in a few more regards. For point groups, D denotes dihedral, and C denotes cyclic groups. The dihedrals have rotational and reflectional symmetries, and cyclic point groups have rotational symmetry about a single axis. For the space groups, P denotes the primitive cell and R denotes the rhombohedral cell. The D6h point group is related to the trigonal prismatic coordination in the bulk 2H phase of layered TMDs and 3R phase layered structures as well. These structures have 6-fold rotation symmetry along the axis perpendicular to the layers of TMD molecules and a horizontal mirror plane perpendicular to the rotation axis. The D3h point group of 2H TMDs with an odd number of layers stands for the 3-fold axis of rotation perpendicular to the layers and one mirror plane perpendicular to the axis of rotation. Additionally, the space groups give information about the translational operations like glide and screw dislocation planes.

In the case of trigonal prismatic coordination of atoms, the P63/mmc space group of multilayered (or bulk) structures, 63 denotes the 6-fold screw axis (6-fold rotation with a translation parallel to the rotation), /m is perpendicular to the screw axis and m is the mirror plane parallel to the screw axis. The c in the end represents the glide plane with a glide vector perpendicular to the layers.[61–63]

The symmetry reduces in the case of monolayer H TMD materials to $P\bar{6}m2$ with a 6-fold rotational axis with inversion symmetry, mirror plane perpendicular to the layers, and a two-fold rotation axis perpendicular to the roto-inversion axis. The R3m in the case of rhombohedral 3R phase means that there is a 3-fold rotation symmetry, and a mirror plane perpendicular to it.

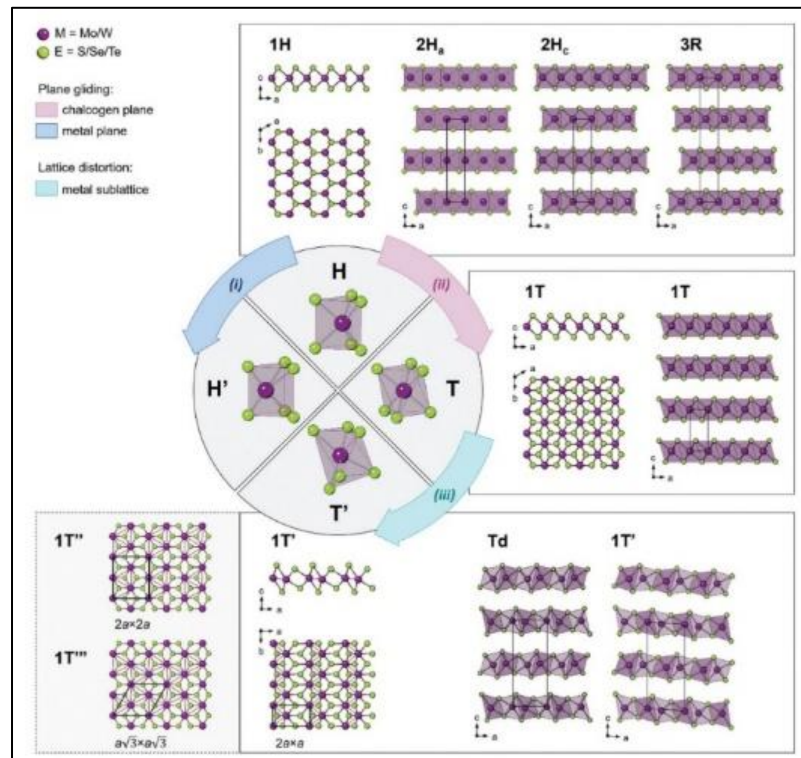

Figure 1.3. TMD structures: (a) top view of layered TMDs; (b) side view of layered TMDs.[43]

In the case of 1T TMDs, the D3d point group suggests they have a 3-fold inversion symmetry around the central metal atom site “b”, and a mirror plane perpendicular to the inversion axis. The space group P$\bar{3}$m1 represents this as P stands for the primitive cell (hexagonal, in this case), threefold rotation axis combined with an inversion center, m represents the mirror plane is perpendicular to the threefold rotation axis and 1 represents one of each of the symmetry elements.[64,65] This is observed in the case of the octahedral coordination of TMDs or trigonal prismatic for an odd number of layers. For the P21/m space group under the same point group, 21 suggests the 2-fold rotation axis perpendicular to the layers with an inversion center and mirror plane. Lastly, the 1Td orthorhombic structure shows Pnm21 space group implying a glide plane, mirror plane, and another glide plane with translational symmetry. Out of these, some are centrosymmetric while others are non-centrosymmetric, and this results in unique electronic behavior which will be discussed in the later sections.

Typically, the groups 5 and 6 transition metals lead to a D3h point group of the crystal structure and the groups 4, 7, and 10 ones lead to the D3d point group. The point groups represent the most probable coordination of the chalcogens- hexagonal in the case of D3h and octahedral in the case of D3d.[66–69]

Phase	**Stacking order**	**Crystal system**	**Point group**	**Space group**[56]	**Coordination**
1H; 2H ($2H_a$); $2H_c$	AbA (1 layer); AbA BaB; AcA BcB;	Hexagonal	D_{6h} (bulk) or D_{3d} (odd number of layers) D_{3h} (even number of layers)	$P\bar{6}m2$ $P6_3/mmc$	Trigonal prismatic.[70]
1T; $1T_d$; 1T’	AbC AbC	Tetragonal; Orthorhombic; Monoclinic	D_{3d} C_{3v} C_{2h}	$P\bar{3}m1$ Pnm21 $P2_1/m$	Octahedral; Octahedral;[67,71] Distorted octahedral.[72]
3R	AbA BcB CaC	Rhombohedral	D_{6h} (bulk)	R3m	Trigonal Prismatic.[43]

Table 1.2. Stacking order, crystal system, point groups, space groups, and metal atom coordination for different phases of TMDs

Chapter.2. Materials in this study

In this study, we focus on the Mo-based TMD materials with S, Se, and Te chalcogens forming an $MX_2$2D structure. Given the structural similarity across these materials, specifically under the MX_2framework, certain analyses described in this section can be extrapolated across the entire family, aiding in our comprehension of their properties. Interestingly, with the same transition metal and increasing atomic size of chalcogens, the bandgap decreases, due to the broadening of d-bands.[44,48,73] This is an important distinction between the materials that impart their specific properties.

The bonding of transition metal and chalcogen atoms can be explained using ligand complex theory.[51,54] In the structure with a metal atom coordinated with six neighboring chalcogen atoms, we will consider the d electrons of transition metals and the p electrons of the chalcogens. The structures, phases, and properties of materials of interest in this study are discussed further below.

2.1. MoS_2

MoS_2 is a widely studied TMD material. It has been used for a long time, starting as a lubricant material to sophisticated photovoltaics today.[74] In the intralayer bonding of one Mo and two S atoms, all the sulfur electrons and most of the molybdenum electrons fill up the bonding orbitals. The interlayer bonding or interfacial bonding is thus a result of the electrons in antibonding orbitals and these have higher energy.[74] The molecular orbital diagram shows the six electrons in Mo and 4 electrons in each of the two S atoms forming bonding and antibonding orbitals.

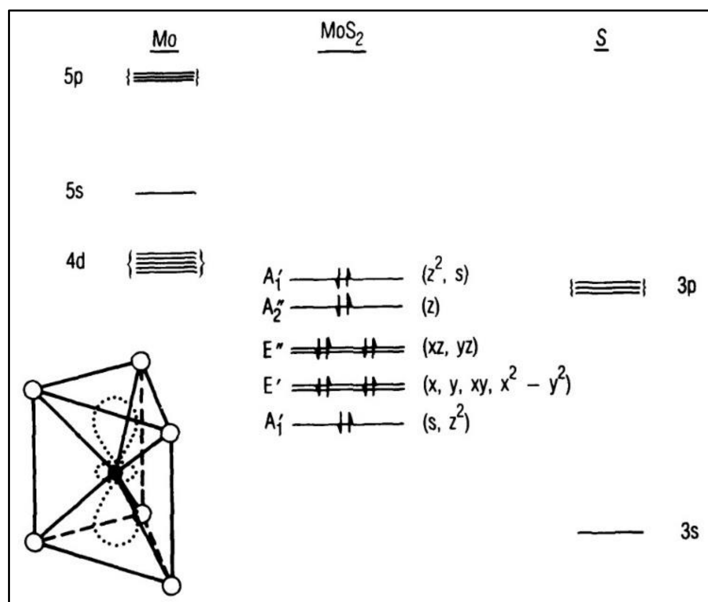

Figure 2.1. Molecular orbital energy-level diagram of 2H MoS_2.[75]

Starting with the lowest energy A1', E', and E", these form the bonding orbitals that lead to the occupation of 10 electrons from 5s and 4d orbitals of Mo and 3p orbitals of S atoms. The next A_2" orbital is filled with two electrons from the pz orbitals of S atoms as they do not hybridize with Mo orbitals. Lastly, the A_1' closer to the Fermi energy level, has some S character, but mostly is Mo antibonding orbital and is filled with two electrons as well. As such, the 14 electrons are involved in the MoS_2 bonding. The interlayer bonding is left to the higher energy unoccupied E' and E" orbitals which have both Mo and S character.

Orbital	**Metal orbitals**
A_1'	5s, $4d_{z2}$ or, s, z^2
E'	$4d_{xy}$, $4d_{x2-y2}$, 5_{px}, 5_{py} or, xy, x^2-y^2, x, y
E"	$4d_{xz}$, $4d_{yz}$ or, xz, yz
A_2"	$5p_z$ or, z
A_1'(bottom)	$4d_z^2$, 5s or, z^2, s

Table 2.1. The character of orbitals energy-level and respective contribution of the metal orbital.[76]

A similar analysis can be extended to the trigonal prismatically or octahedrally coordinated structures. The metal atoms in TMDs can be coordinated in the two different types and correspondingly, the d orbital division and location of the Fermi energy level differs. The d orbitals of the octahedrally coordinated transition metal atoms are divided into three energy levels that in ascending order of their energy are one- dz2, two- dx2-y2 and dxy, and three- dxz and dyz. Similarly, the octahedrally coordinated transition metal atom has the five d orbitals split into two energy levels, one- dyz, dxz, and dxy, and two- dz2 and dx2-y2. The Fermi energy levels lie within these orbital levels as shown in the diagram below.[77] In the upcoming section, several pathways to phase transition will be discussed.

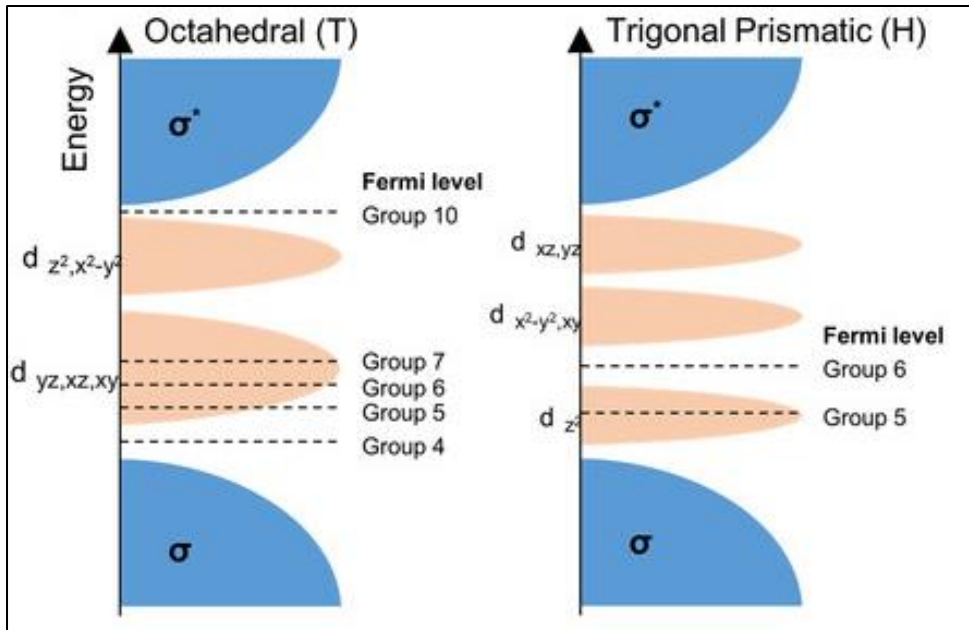

Figure 2.2. d orbitals splitting in transition metal atoms with respect to the coordination and the related Fermi energy level.[78]

2.2. $MoTe_2$

Each Mo atom is coordinated to 6 Te atoms in a trigonal prismatic fashion in 2H-$MoTe_2$. The two tetrahedrons with Mo bonded to its Te ligands are stacked symmetrically in a layer. In the 2D form, multiple layers can be stacked by edge-sharing of the trigonal prisms. As discussed in the previous section, the 1H phase has a hexagonal crystal symmetry, 2H has an additional hexagonal screw rotation, and 3R with three-fold rotation symmetry. The 1Td is an octahedrally coordinated structure with tetragonal symmetry. Here, one of the two tetrahedra in the stack is 180° rotated with respect to the other one. In the 1T' phase, the primitive cell is a rectangle in the X-Y plane making it monoclinic in symmetry. In the tetrahedral structure, one is 180° rotated and the stack is distorted. The distortion occurs as the transition metal atoms in 1Td undergo dimerization and results in distortion of the chalcogen atoms shifting them out-of-plane. This changes the overall symmetry from three-fold to two-fold.[79]

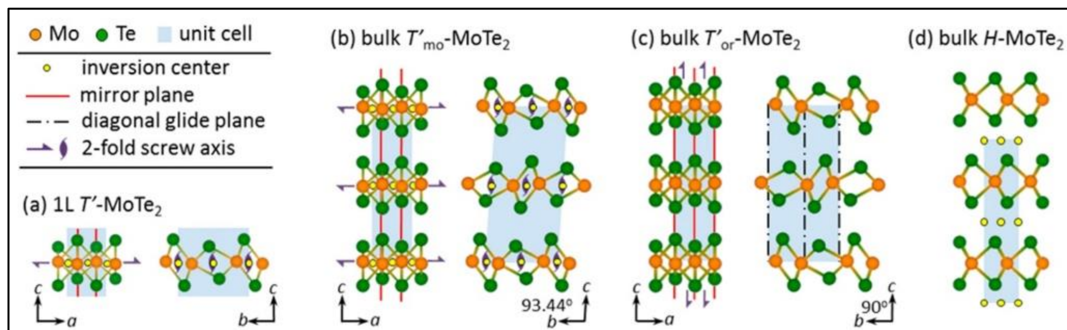

Figure 2.3. (a) 1T' $MoTe_2$ monolayer crystal structure and the related crystal symmetries. (b) Bulk monoclinic 1T' $MoTe_2$ and the related crystal symmetries. (c) Bulk orthorhombic 1T' $MoTe_2$ and the related crystal symmetries. Bulk hexagonal $MoTe_2$ and the related crystal symmetries.[79]

The 2H $MoTe_2$ monolayers exhibit a direct bandgap of 1.1 eV and multilayers exhibit an indirect bandgap of nearly 1 eV. These energy values translate to wavelengths that fall on the near-infrared region of the electromagnetic spectrum and are therefore one of the star candidates for optoelectronic applications.[80,81] The current challenges in the growth of a controlled phase of $MoTe_2$ will be discussed in the upcoming sections. This method can also be used to synthesize $MoSe_2$. Overcoming the growth limitations and characterization of the 2D films is the area of research targeted in this thesis. The strength of the growth methods discussed here is the ability to grow the materials on multiple substrates and as heterostructures in a controlled manner. SiO_2, Si, and GaN substrates are used to grow the TMDs here.

2.3. Bandgaps, Brillouin zone, and Lattices

2.3.1. Materials and bandgaps:

The energy bandgap (Eg) is an important property of materials that needs investigation for electronics research and applications. Eg is the separation between the valence band and the conduction band, thus representing the energy barrier between the highest occupied energy level and the lowest unoccupied energy level of materials. The band theory explains the different materials with regard to their bandgap as follows:[82,83]

1. Metals: the valence band and the conduction band overlap, or are very close in energy. The Fermi level lies within the conduction band for metals or they have no energy gap. Electrons in metals can easily move from the valence band to the conduction band with very little energy input, facilitated by thermal energy. This abundance of free electrons allows metals to conduct electricity very effectively.
2. Semimetals: the overlap between the valence and conduction bands is very small or they have a very small energy gap between them. The Fermi level lies within the small energy gap between the valence and conduction bands. Semimetals exhibit properties that are intermediate between metals and semiconductors. They can conduct electricity better than insulators but not as effectively as metals.

3. Insulators: they have a large energy gap (bandgap) between the valence and conduction bands. This bandgap is typically greater than 3 eV. The Fermi level lies within the bandgap, far from the valence and conduction bands. Insulators have very low electrical conductivity because the energy required for electrons to move from the valence band to the conduction band is extremely high. Consequently, they cannot conduct electricity under normal conditions.
4. Semiconductors: they have a moderate energy gap (bandgap) between the valence and conduction bands due to a finite separation between the two bands. The Fermi level lies within the bandgap, closer to the valence band for intrinsic semiconductors (pure) and closer to the conduction band for doped (extrinsic) semiconductors. At room temperature, semiconductors have a low electrical conductivity because most of their electrons are in the valence band. However, they can conduct electricity when provided with additional energy, such as heat or light, which enables electrons to move from the valence band to the conduction band.

The semiconductor bandgap can be direct or indirect. In 2D TMDs, the monolayers exhibit a direct bandgap and multilayers exhibit an indirect bandgap. The direct bandgap is usually smaller than the indirect bandgap. The direct bandgap exhibited by TMDs is less than 1eV which can be tapped for applications using near-infrared (NIR) electromagnetic (EM) signals.[80,84,85] This is important as a small bandgap is more desirable for optoelectronics applications.

2.3.2. Energy levels in TMDs

In a molybdenum (Mo) based TMD molecule, the bonding arrangement involves Mo contributing 6 valence electrons, out of which the 4 valence electrons from Mo occupy the bonding states primarily from the p valence orbitals from the chalcogens. The d orbitals of Mo experience splitting due to the surrounding environment, leading to distinct energy levels occupied by the last two electrons from Mo.[85,86] In trigonal coordination, the semiconducting properties come from the completely occupied conduction band, and the octahedral coordination configuration gives the materials semimetallic properties due to an incompletely filled conduction band.[85–87] In the semiconducting phase, the completely filled conduction bands cause the absence of energy states that could be occupied by free electrons under normal conditions. In the semimetallic phase, the incompletely filled conduction band allows for the flow of free electrons via the available energy levels thus conducting electricity.[88]

The splitting of 4d orbital of Mo can result in three energy levels: one non-degenerate orbital at the lowest energy level; and two doubly degenerate orbitals at higher energy levels.[85] The Fermi energy level lies between these two bands. For example, in the 2H MoS_2 monolayer, the highest occupied molecular orbital (HOMO) primarily consists of Mo dz_2 orbitals, filled with two paired electrons. The lowest unoccupied molecular orbital (LUMO) mainly consists of Mo dx2-y2 and dxy orbitals, situated 1.9 eV above the HOMO.[88] This is the optical (direct) bandgap of monolayer MoS_2 (D3h symmetry) that can be observed in photoluminescence (PL) spectroscopy. While in the MoS_2 with (D3d symmetry) semimetallic properties, the 4d orbitals split only into two- a triply degenerate band, labeled t2g at a lower energy level, and a doubly degenerate band, labeled eg at a higher energy level.[88] The Fermi energy level in this case is at the triply degenerate t2g level. This is the partially filled energy level that results in electrical conduction.[88]

2.3.3. Bandgap and Brillouin zones

The Brillouin zone represents the reciprocal space of a crystal lattice. In reciprocal space, the wave vectors represent different points. Understanding this representation is important for analyzing electron behavior in a periodic lattice. The first Brillouin zone is the smallest unit cell in reciprocal space that, when repeated, constructs the entire reciprocal lattice.[65]

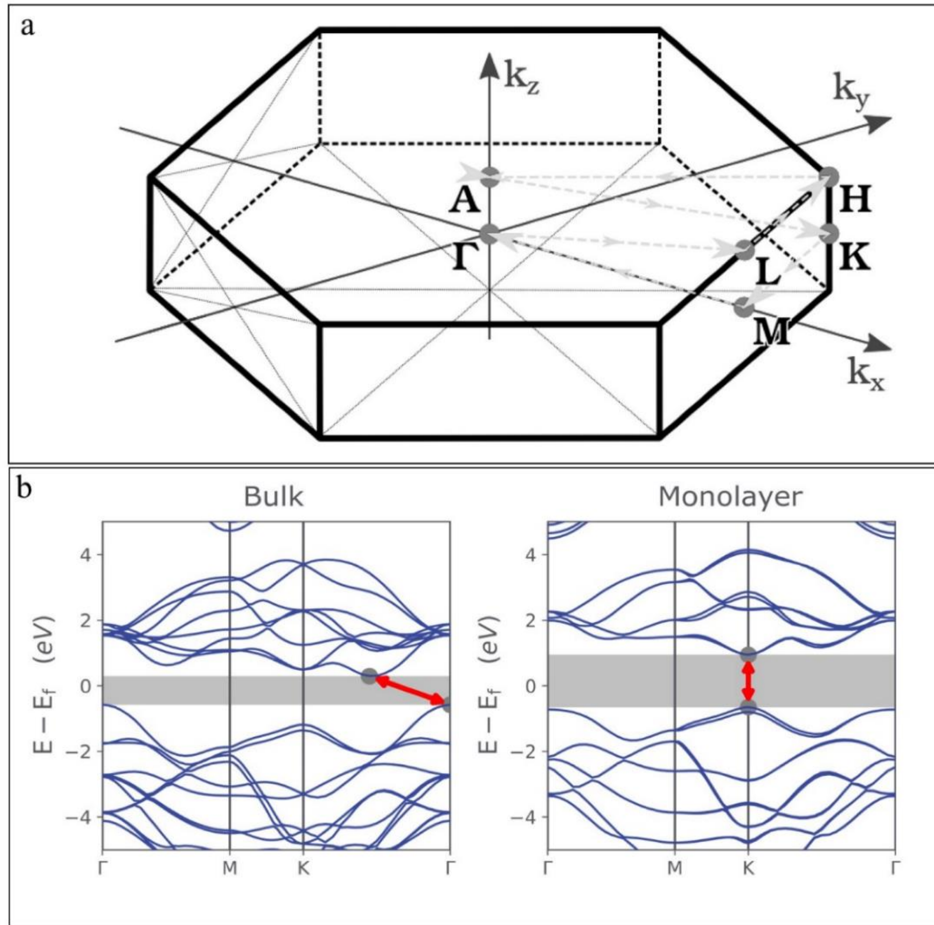

Figure 2.4. (top) and Brillouin zone of 2H MoS_2; energy band structure of 2H MoS_2 (bottom-left) bulk; (bottom-right) monolayer. The red arrows show the indirect bandgap between conduction band minima and valence band maxima.[89]

MoTe2	MoS2	GaN	SiO2/Si
2H = 3.56 1T' = 3.49	3.19	3.22	5.11

MoTe2/SiO2	MoTe2/MoS2	MoS2/GaN
2H → 43%	2H → 11.59%	0.94%
1T' → 46.4%	1T' → 9.4%	

Table 2.1 Lattice constants and % mismatch for $MoTe_2$, MoS_2, GaN and silicon.

The center of the Brillouin zone is the Γ point.[90,91] It is the highest symmetry point. The K point is at the edge of the Brillouin zone along high symmetry axes and it connects the corners of the Brillouin zone. The M point is at the midpoint of the edges of the Brillouin zone but not along the high-symmetry axes. The A point is located at the top or bottom face of the Brillouin zone, representing a vector perpendicular to the basal plane in real space. It is the high symmetry point above the Γ point. Similarly, the L and H are points above the M and K points.[92] The conduction band exhibits local minima at certain points in the Brillouin zone known as low symmetry Q points, also referred to as Λ points. These Λ points are distinct from the high-symmetry points like the Γ and K points and typically arise due to the TMD material's specific crystal structure and electronic properties.[93–96] The T point is located between the Γ and K. It is a lower symmetry point compared to other high symmetry points.[96] The electronic band structure of a material, which describes the allowed energy levels (bands) for electrons in the crystal, is typically calculated within the Brillouin zone. The electronic states and their energies at different points within the Brillouin zone provide insight into the material's electronic properties, including its bandgap. The bandgap of materials can be directly observed in the band structure plot within the Brillouin zone. Apart from such electronic structure analysis, it can also be used to study quantum confinement effects, strain engineering, topological properties, heterostructure design, and optical properties of TMDs.[84,97–99] For example: the hexagonal lattice structure of 2H TMDs when rotated by 90° resembles the hexagonal reciprocal lattice structure. This makes the first Brillouin zone as shown in Figure. 2.1.[100] The conduction band minima and valence band maxima lie at the K points for monolayer

TMDs and between the Γ and K points for the multilayer TMDs.[96] These transitions are typically important for electrons that can go from the ground to an excited state with the absorption of energy and relax to the ground state by emission of the energy. Similarly, other particles that can be studied are excitons, phonons, polaritons, and other quasiparticles.[92,101–104] The irreducible representation of symmetry groups and selection rules can explain the lattice vibrations in TMD crystals. The Raman scattering, which can be used to obtain information about the lattice vibrations, can be either a first-order or a second-order process. The first-order process occurs at the Γ point and the second-order processes at the M and K points.[105,106]

2.4. Phase transition

The TMD structure phase is determined by growth conditions or applying external stimuli post-growth. During growth, the important factors that determine the phase of the material are the temperature, relative fluxes of transition metals and chalcogens, availability of precursors, dopants, and substrates. The 1T phase can undergo further distortion as the degeneracy of the d orbitals is broken and two of the three bonding orbitals occupy lower energy levels as the symmetry of the structure reduces.[77,107] The transition mechanism can be interpreted with thermodynamic or kinetic transition. Due to the energy barrier between the two phases, intermediate phase formation can take place that offers conducive conditions for the transition or atomic deficiencies that make the transition easier.[77]

A particular structure can be preferentially stabilized over another by charge doping. Two possible reasons for this are: one, the introduction of excess charge reduces the metal-chalcogen bond strength, making the plane gliding easier; two, the splitting of d orbitals is changed which affects the metal coordination and the overall phase. Charge doping, intercalation, and laser irradiation are some of the methods that can be used to achieve this.[77,98,107–114] It should also be noted that in TMDs with a group VI transition metal, the energy barrier between the phases reduces as the chalcogen atomic weight increases down the periodic table.

Chapter.3. Growth and characterization methods

3.1. Growth methods

The 2D TMDs can be grown by top-down and bottom-up synthesis routes. With top-down synthesis, the source material is a bulk TMD that is made thinner by mechanical or chemical techniques of separating layers that can then be deposited on required substrates. The term bottom-up synthesis applies to methods that use chemical precursors or physical evaporants used to make 2D films of the desired composition. Most commonly used growth methods under these two classifications are briefly explained below.

3.1.1. Top-down synthesis:

1. Scotch Tape Method (Mechanical Cleavage or Exfoliation): This simple yet effective technique involves using adhesive tape to peel off layers from the bulk TMD material. By repeatedly sticking and peeling the tape, thinner and thinner layers can be obtained, eventually reaching the monolayer or few-layer thickness. This method is renowned for producing layered structures and can be modified by using different adhesion mechanisms like a visco-elastic silicone stamp or exfoliation by rubbing.[115,116]
2. Metal-assisted exfoliation method: Metal-assisted exfoliation involves depositing a thin layer of metal onto the surface of bulk TMD material. Upon applying external stimuli such as heat or chemical agents, the metal layer helps peel the TMDs that are bonded to the metal via van der Waals forces. Gold (Au) has been proven to be useful in this method with the inclusion of thermal release tape.[117]

3. Gel-Assisted Exfoliation: The gel-assisted exfoliation method involves using a gel film to transfer exfoliated 2D TMDs from one substrate to another. The method relies on the correlation between the separation rate and adhesion between the gel film and the substrate when external forces are applied. If the adhesive force of the gel film is greater than the Van der Waals interactions between the substrate and the 2D TMD, successful transfer can be achieved. This technique offers transparency, ease of handling, and flexibility in transferring exfoliated materials to designated substrates.[118]
4. Layer Resolved Splitting: This method is a novel technique for isolating large-area monolayers of transition metal dichalcogenides (TMDs), such as WS2, in a scalable manner. Developed by Shim et al., LRS involves the use of chemical vapor deposition (CVD)-grown TMD multilayers on a substrate. A thick nickel (Ni) film is deposited on both the top and bottom surfaces of the multilayer TMD. By sequentially depositing and detaching Ni layers, monolayer TMDs are split from the bottom up. Although the quality of monolayer samples from LRS may not match that of traditional methods like the Scotch tape method, LRS represents a significant advancement in producing wafer-scale monolayer TMDs.[119]

5. Ball Milling: In this process, bulk TMD material is placed in a hollow cylinder along with grinding balls. As the cylinder rotates, the balls collide with the material, gradually exfoliating it into thinner layers. Ball milling can be used to produce large quantities of material, but the control over thickness and uniformity is less precise compared to methods like mechanical cleavage. Despite this, it's a versatile technique that can be adjusted by varying the milling time and speed, ball size, material-to-ball ratio, and even the milling agent, allowing for some degree of customization in the resulting material properties.[120,121]
6. Ion intercalation: The ion intercalation method for exfoliating bulk transition metal dichalcogenides (TMDs) involves inserting impurities between the layers of the TMD crystal to expand the interlayer space, thereby reducing the van der Waals forces and lowering the energy barrier to exfoliation. Various intercalants such as alkali metals, organometallic compounds, polymers, and atomic species are used, with lithium ions being particularly effective due to their high reduction potential and mobility. The process typically uses n-butyllithium (n-BuLi) in hexane, where n-BuLi donates an electron to the TMD layers, allowing Li+ ions to intercalate and maintain charge balance. Techniques like ultrasonication or microwaves enhance the efficiency of lithium intercalation. The lithium-ion-intercalated TMD crystal is then exfoliated into nanosheets through hydrolyzing and sonication.[122,123]

7. Solvent-based exfoliation: The solvent-based exfoliation method for producing 2D materials involves four main steps: immersion, insertion, exfoliation, and stabilization. This method requires the 2D material to be fully immersed in a solvent that facilitates efficient exfoliation during sonication, prevents the restacking of exfoliated materials, and maintains a high concentration of the exfoliated material. The choice of solvent is critical and is determined by considering factors such as surface tension, and solubility parameters to ensure compatibility with the specific 2D material.[119] A recent study shows laser-assisted solvent-mediated exfoliation where TMDs are exfoliated using a homemade femtosecond laser system, focusing high-power laser on bulk TMD materials (e.g., $MoSe_2$, MoS_2, WS_2, WSe_2) dispersed in deionized water for 1 hour. This separates TMD layers, yielding few-layer TMD flakes (100-200 nm thick). Optimizing laser power (1.2 W) and irradiation time prevents sample damage. The method enables mass production of homogeneous few-layered TMDs, ideal for large-area optoelectronic devices like photodetectors and photovoltaics.[124]

3.1.2. Bottom-up

1. Chemical Vapor Deposition (CVD): the CVD process can be an atmospheric pressure-based or lower pressure-based growth mechanism. The gas flow in the reactor furnace controls the pressure. Depending on the materials, the process can be single or multi-step. Some modified CVD growth methods can also be used to grow heterostructures laterally or vertically stacked. The synthesis mainly involves chemical reactions between precursors. In thermal CVD, powder forms of transition metal oxides and chalcogens are utilized. Heating these precursors causes evaporation, and subsequent adsorption onto substrates for TMD formation. The ratio of transition metal to chalcogen, growth temperature, and edge structure influence TMD shape evolution. In the two-step method, a metal oxide film is deposited first and then it is exposed to chalcogen vapor to synthesize TMDs.[125–127]

    i) Chemical Vapor Transport (CVT): CVD involves chemical reactions of gas-phase precursors on or near the heated substrate surface, leading to the deposition of a solid material. CVT, in contrast, relies on the transport of material in the vapor phase from a hotter zone (source) to a cooler zone (growth area) within a sealed container, facilitated by a carrier gas or a chemical transport agent.[128]

ii) MOCVD: In MOCVD, growth is carried out by introducing organic molecule gases containing transition metals (Mo or W) and chalcogens (S or Se) over a substrate, decomposing them with thermal energy to deposit TMD thin films. This method allows control of precursor partial pressures, enabling uniform deposition on large substrates. While MOCVD offers precise layer control and large-area uniformity, it requires toxic precursors and expensive equipment. With proper conditions, it can produce wafer-scale monolayers with homogeneous properties.[119,128]

2. Atomic Layer Deposition (ALD): In ALD, metal and chalcogen precursors are alternately introduced into a reaction chamber and purged with an inert gas between each feeding to prevent intermixing. Each ALD cycle involves exposure to metal precursor, purging, exposure to chalcogen precursor, and purging, resulting in linearly increased film thickness with ALD cycles. Large-area growth of monolayer and few-layer MX_2 films with high uniformity has been achieved using various precursors.[129]

3. PLD: By directing nanosecond pulses of an ultraviolet laser onto a target, small molecular clusters are vaporized to create a plasma plume that deposits onto substrates. PLD can be conducted in a vacuum or low-pressure gas ambient, with reactive PLD occurring in gases like oxygen or nitrogen. Plasma beams can be incorporated to enhance interactions. The quality of PLD-deposited samples depends on the laser wavelength and energy, affecting plasma absorption and resulting in photothermal ablation, which can impact film phase formation. Shorter wavelengths reduce plasma heating effects, but maintaining low laser energy minimizes photothermal ablation.[124,130]

4. Physical Vapor Deposition (PVD): Given the high melting temperatures, the evaporation of transition metals requires excessive energy. As such, the PVD type of growth is vacuum-based. Methods like eBeam evaporators, plasma, or sputtering are typically used for transition metal evaporations and thermal evaporation of chalcogens is relatively straightforward.[131]

   i) Molecular Beam Epitaxy (MBE): This technique is conducted under ultrahigh vacuum conditions where epitaxial deposition of thin film crystals on crystalline substrates is achieved using vapor sources like effusion cells. These contain solid sources that are heated and evaporated, generating separate beams of element vapors that are deposited on a substrate to form thin films. MBE systems typically include a Reflection High-Energy Electron Diffraction (RHEED) system for in situ monitoring of crystal growth.[132–134]

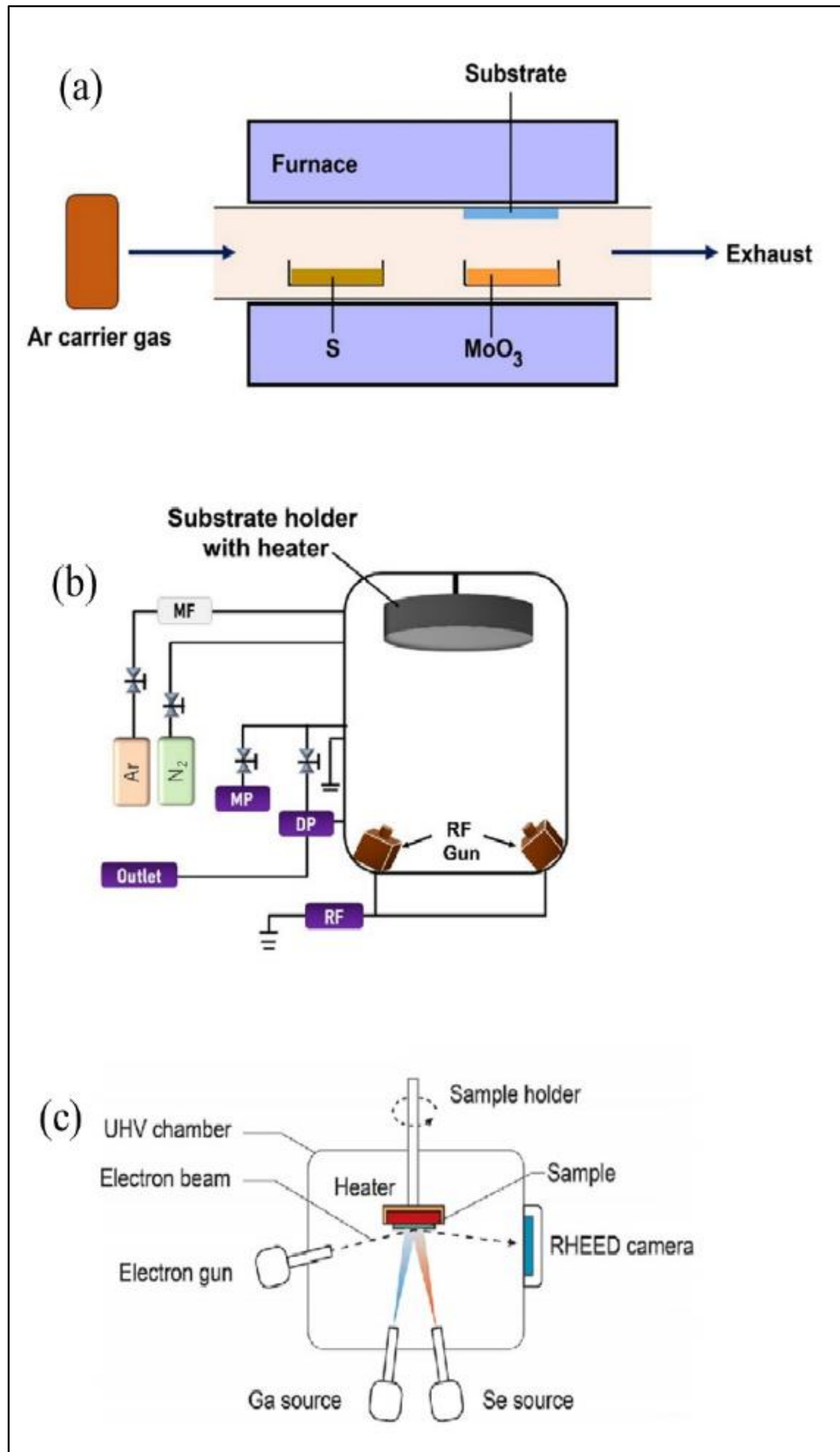

Figure 3.1. CVD growth system; (b) Sputtered growth system; (c) MBE growth system

ii) Sputtering: In this process, atoms are ejected from a solid target material when it's hit by energetic particles like ions or atoms. It relies on momentum transfer from these particles to the target material through collisions. The sputter yield, indicating the average number of atoms ejected per incident particle, depends on factors like ion angle and energy, ion and target atom masses, target surface binding energy, and target crystalline orientation. PVD via sputtering can be achieved using DC, AC, RF, and Magnetron sputtering. In DC, a potential across the substrate and target generates plasma when gases are introduced. AC and RF setups avoid issues like positive charge buildup and are suitable for insulating targets. Magnetron sputtering enhances deposition rates at lower pressures by using electric and magnetic fields to generate more ions near the target surface, increasing sputtering and deposition rates. RF is advantageous, particularly for insulating targets, as it reduces electron bombardment and substrate heating.[135,136]

In this study, we use the co-deposition of transition metal via e-beam evaporation and chalcogen via thermal evaporation in the UHV system to make $MoTe_2$ and $MoSe_2$. MoS_2 growth is based on Almeida et. al.[137] Both of these will be discussed in detail in upcoming sections.

3.2. Characterization techniques

3.2.1. Raman Spectroscopy

1. Theory

Atoms in molecules are in a state of motion depending on their energy and the degrees of freedom inherent in molecular structure. This motion is influenced by various factors, like temperature and external electromagnetic excitations. The degrees of freedom of a molecule are determined by its linearity or nonlinearity, as well as its rotation and reflection symmetries. For non-linear molecules comprising N atoms, the degree of freedom is given as 3N-6.[138,139] For TMD molecules like $MoTe_2$ or MoS_2, it would be 3*3-6 = 3. Consequently, these molecules can undergo symmetric or asymmetric stretching and bending motions relative to their molecular geometry. The EM waves incident on the molecules can interact with their atoms and result in different phenomena ranging from no change to scattering, absorption, emission, or photoluminescence.[139–141] Changes in the vibrational, rotational, or electronic energy states of the atom cause this.

Raman scattering, a particular type of inelastic light scattering, emerges from molecular vibrations. When incident laser light interacts with molecules, it energizes them, inducing vibrational motion in an excited state. These vibrational modes, especially in crystalline materials, are quantized and are referred to as phonons.[138,139,142]

After this excitation, the molecules gradually return to their stable ground state, emitting energy in the form of scattered light. The frequency of this scattered light typically decreases compared to that of the incident light in cases of inelastic scattering. It is influenced by the molecular vibration and rotation frequencies, mediated by phonons in crystalline materials, potentially leading to a return to either the original ground state or a higher energy state. This frequency shift can be determined by adding the molecular vibration frequency to the incident frequency, resulting in Stokes lines, or by subtracting the two, yielding anti-Stokes lines. These energy transitions correspond to vibrational and rotational levels, distinct from higher-energy electronic transitions. Raman spectroscopy thus provides valuable insights into molecular structure and dynamics, operating on energy scales separate from those of electronic transitions.

Additionally, molecules as a whole, not just individual atoms, absorb the energy of the incident photons, leading to vibrational excitation. The relaxation process involves the molecule transitioning from the excited state to a lower energy state, typically the ground state, through the emission of photons. These emitted photons constitute the scattered light. In principle, if the frequency of incident light is known, from the Stokes and anti-Stokes lines, the vibration frequency of the molecule can be inferred.

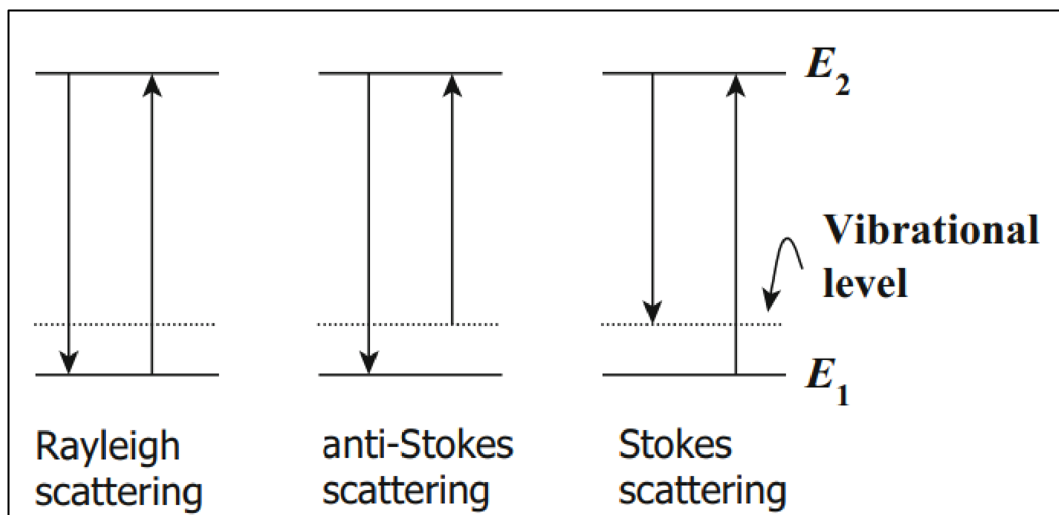

Figure 3.2. Electron relaxation mechanisms- Raleigh scattering, anti-Stokes scattering, and Stokes scattering.[82]

2. Instrumentation

In a typical Raman spectroscopy setup, a laser serves as the light source to excite the sample, while a detector collects the Raman scattered light. Additional optics, like mirrors and lenses, focus the beam and optimize the setup for improved signal quality. A basic setup may include an Nd:YAG laser, mirrors for alignment, right-angle prisms for folding the beam, and an achromat lens for focusing the light onto the sample. The scattered light is then collected and focused onto the detector for analysis.[143–145]

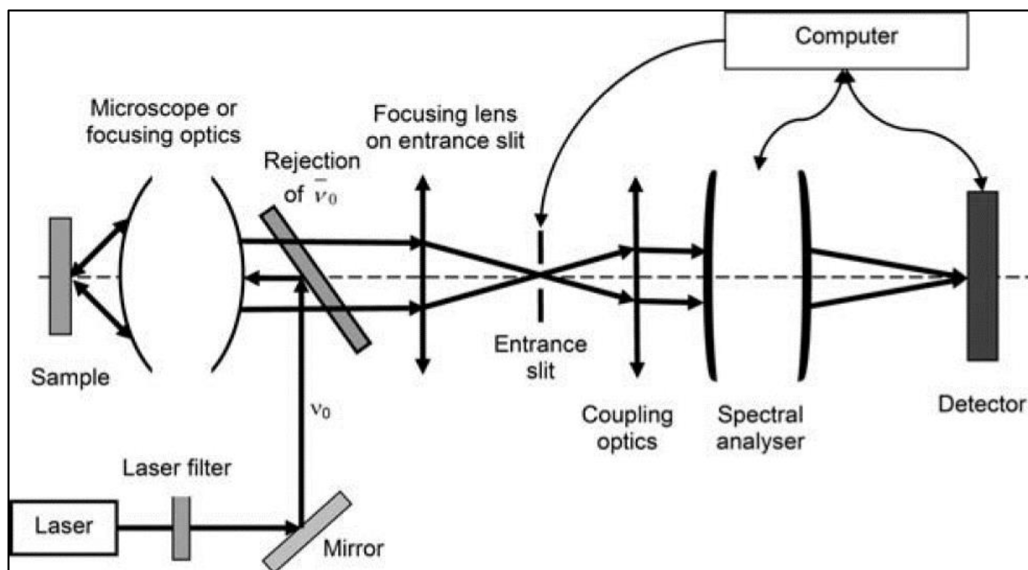

Figure 3.3. Simplified representation of Raman instrumentation.[146]

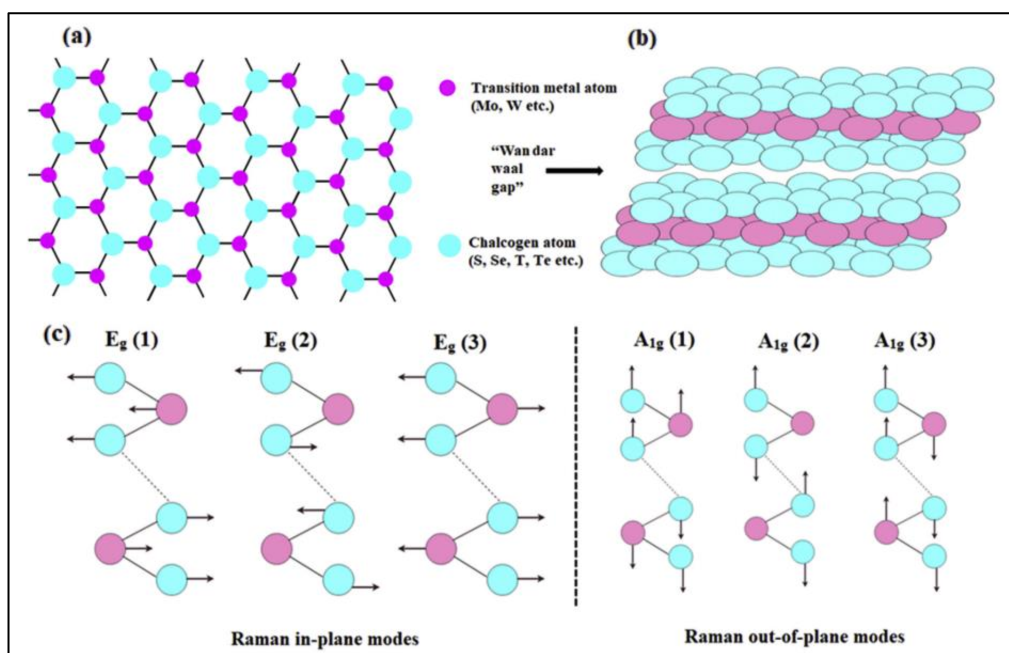

Figure 3.4. Raman vibration modes of TMDs: (a-b) TMD structures; (c) in-plane and out-of-plane modes.[147]

Key considerations in Raman spectroscopy setup include laser power, signal-to-noise ratio (SNR), detector selection, and filtering. NIR lasers are often preferred to avoid sample fluorescence, while detectors with high quantum efficiency are chosen based on the laser wavelength used. Filtering ensures that only the desired signal is detected, enhancing measurement accuracy. To detect which frequencies of light were absorbed by molecules, we measure the frequency shift between the original light beam and the Raman scattered light. This shift, known as the Raman shift, provides crucial information about the sample's molecular composition. Using a monochromatic laser, such as a green laser at 532 nm, ensures precise determination of the original light beam's frequency, as lasers emit light of uniform wavelength and frequency providing a unique "fingerprint" by which the sample can be identified.[148]

3.2.2. Photoluminescence Spectroscopy

1. Theory

The molecules absorb incident photons and result in the excitation of electrons from their ground states to a higher excited electronic state. These electrons can relax back to their ground states by emitting photons. This is the principle of photoluminescence. [82]

The PL in TMDs stems from the recombination of electrons in the conduction band with holes in the valence bands, which are split by spin-orbit interactions. This combination leads to light emission and is marked by specific features identified as the A-peak or the B-peak. The A-peak represents the ground state exciton and the B-peak represents a state with higher spin-orbit splitting. The ratio of intensities between these peaks indicates the sample quality, where a lower B/A ratio suggests fewer defects and higher quality.[149–151] The PL peak is affected by the defect densities, thickness of layers, strain, edge effects, as well as external stimuli and doping. In the case of TMDs, many-body complexes like excitons, trions, neutral biexcitons, and chared biexcitons can be measured using PL spectroscopy.[152,153]

2. Instrumentation

A generic PL spectroscopy setup has a light excitation source, detector, optical and electronic systems to process the signals, and a display setup. The power and wavelength of the light source depend on the measured sample. Optical setup can be used to focus on an area to measure the PL and the emitted signal is sent to the spectrograph where the light-sensitive detector captures the signal. The signal is further processed using optical and electronic systems for better analysis with required calibrations.[150,151,153]

3.2.3. X-ray Photospectroscopy

1. Theory

X-rays are high-energy EM waves compared to visible light and UV rays. They can be used in surface analysis of the materials. The XPS spectroscopy operates on the principle of the photoelectric effect, where high-energy X-rays are used to eject core-level electrons from atoms in a sample's surface region.[139] This phenomenon was explained by Dr. Albert Einstein in his Noble award-winning study of the photoelectric effect. XPS provides valuable information about the elemental composition, chemical states, and oxidation states of the top few nanometers of a material's surface. The binding energy of ejected electrons, measured by XPS, reflects the energy required to remove electrons from specific atomic orbitals. Each element has characteristic binding energies for its core-level electrons, enabling the identification of components and their chemical environment.[139,154,155] Moreover, XPS offers quantitative analysis capabilities, allowing the determination of the atomic concentration of elements present in the sample surface. Corrections for factors such as atomic sensitivity factors and electron escape depths are applied to the measured intensities of photoelectron peaks. The kinetic energy ($E_{kinetic}$) of the emitted electron depends on the incident photon energy (E_{photon}), the binding energy of the electron ($E_{binding}$), and the work function (ϕ) which depends on the instrument. This relationship is given as:[155]

$$E_{kinetic} = E_{binding} - \phi - E_{photon}$$

The energy of the incident photon is mathematically related to the frequency (or wavelength) of the photon as product $h*\nu$ (Plank's constant and frequency of incident photon) or $h*c/\lambda$ (c is the speed of light and λ is the wavelength of the photon).

2. Instrumentation

An X-ray source generates the X-rays that irradiate the sample surface. The most common source is an X-ray tube with an anode material, often made of aluminum or magnesium. X-rays are emitted when high-energy electrons from a filament are bombarded on the anode material. The choice of anode material, such as aluminum, determines the energy of the emitted X-rays (e.g., Al Kα line at 1486.7 eV).[155] The chamber is maintained under high vacuum conditions to minimize electron scattering and to prevent sample contamination. The sample stage allows precise positioning of the sample. The electron energy analyzer measures the kinetic energies of the photoelectrons emitted from the sample surface. The two main types of analyzers used in XPS are: hemispherical analyzers and cylindrical mirror analyzers. Both types employ magnetic or electric fields to disperse the emitted electrons based on their kinetic energies, allowing for their detection and analysis. The ejected photoelectrons travel toward the analyzer, where they are energy-segregated based on their kinetic energies. This segregation is achieved by applying a potential difference, called the pass energy, between the inner and outer hemispheres of the analyzer.

Higher pass energies result in lower energy resolution but higher electron counts. The detector system records the energy distribution of the emitted photoelectrons. Depending on the instrument configuration, electron multipliers or channeltron detectors can be used as detectors. The detectors convert the kinetic energy of the photoelectrons into electrical signals, which are then processed and analyzed by the instrument's software.

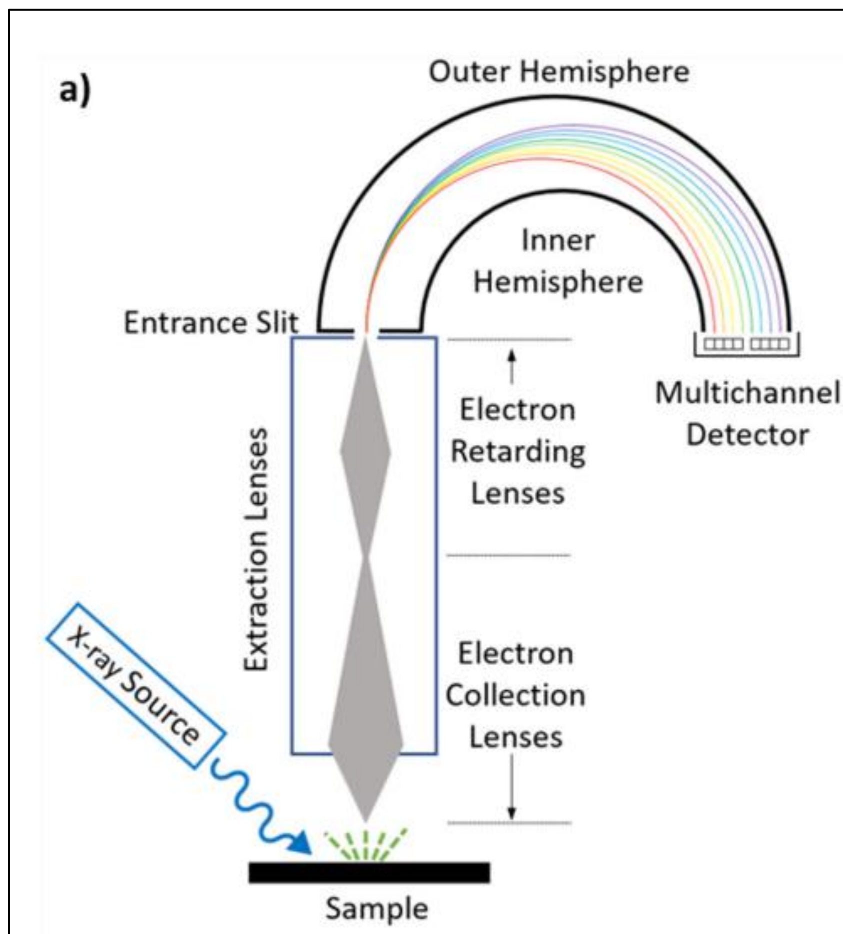

Figure 3.5. Simplified sketch of XPS instrumentation.[155]

3.2.4. Electron Microscopy

a) Theory

Optical microscopy faces a fundamental limitation imposed by the wavelength of visible light, restricting its ability to resolve minute features in materials. As the electrons are smaller in scale than visible light particles, a higher resolution and magnification when imaging matter can be achieved.[156] The smallest distance resolved by an electron beam is given δ.

$$\delta = 0.61/(N.A.)\ \lambda$$

N.A. is the numerical aperture and λ is the wavelength. In the vacuum, the numerical aperture only depends on the angle of the beam collected by the lens. While theoretically, electron microscopy can be used to get resolution in the range of picometers, practical constraints arise from interactions between electrons and samples, as well as potential damage induced by the accelerated electron beams. When electrons interact with matter, the resultant phenomenon depends on material composition, quality, and thickness.[157]

Upon impinging on a material, electrons can be absorbed, generating electron-hole pairs or heat within the sample volume. The portion of electron beams that are not consumed in these interactions can undergo transmission, scattering, or losses. These result in specific characteristic EM waves and more information can be extracted by using correct detectors. If the electron beam can directly pass through a thin sample, such a transmitted beam can be used to obtain bright-field TEM images. And, if the transmitted beams undergo diffraction, those can be used to acquire the dark-field TEM images.

Thicker samples can be cut along their cross sections for using the TEM technique to obtain more than surface information. Scattering events during electron-matter interactions can be either elastic or inelastic, resulting in the production of backscattered electrons or secondary electrons. These phenomena find application in techniques like Scanning Electron Microscopy (SEM), where they are employed to image the surface morphology of the sample and analyze its composition. The X-rays emitted from the sample as a result of incident electrons can be detected to measure the Energy-dispersive X-ray spectroscopy signals. Other events are briefly included in the figure below.[158]

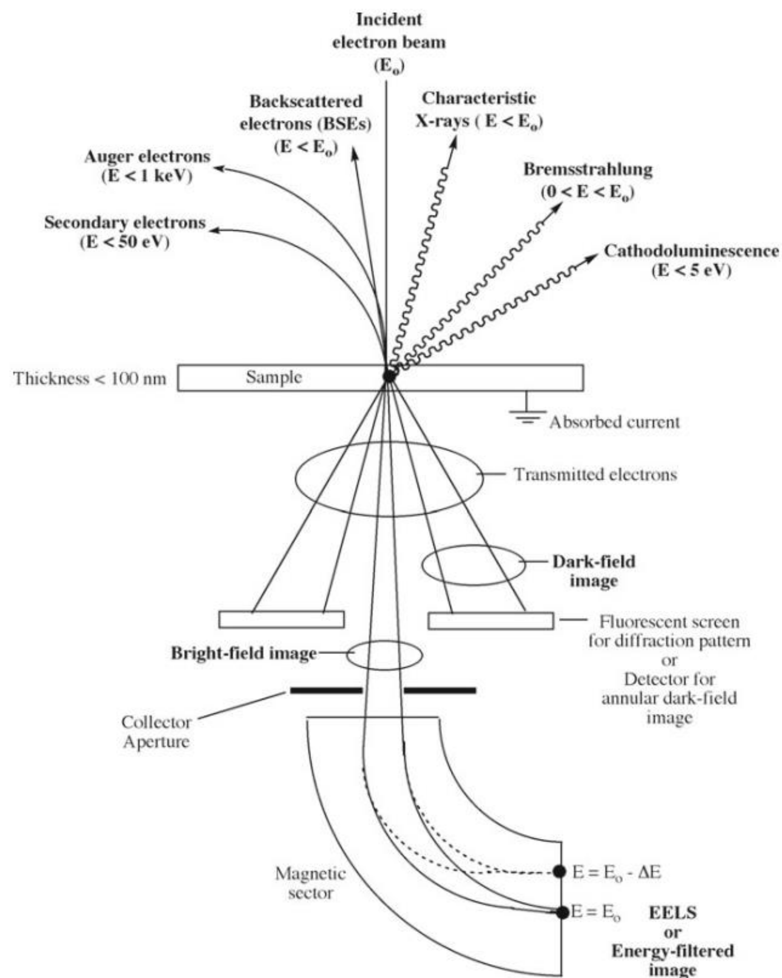

Figure 3.6. Simplified TEM sketch and electron interactions with matter.[158]

b) Instrumentation

The basic equipment for TEM, SEM, and EDS is discussed here briefly. The characterizations take place in vacuum chambers as they avoid contamination and are important for the controlled electron beam generation and direction. An electron beam is generated by heating a tungsten filament via thermionic emission with the application of high voltage. This beam can be shaped and routed using electromagnetic lenses.[139,159] Finally, as mentioned earlier, the detectors play a crucial role in determining the useful data obtained via the electron-matter interactions. They play a pivotal role in determining the characterization of a sample and application, whether it's imaging the sample's surface morphology (SEM), studying its internal structure (TEM), or performing elemental analysis (EDS).[158]

3.2.5. Low Energy Electron Diffraction

1. Theory

Low-energy electrons incident on a sample can measure the reciprocal lattice of the sample surface from its diffraction pattern using the interference pattern of the electrons diffracted from periodically arranged atoms in the sample. In real space, the arrangement of atoms in a crystal can be described in terms of their relative positions using Cartesian coordinates, representing the three dimensions of physical space. In reciprocal space, the crystal structure can be described in terms of the spatial frequencies of its atomic arrangement. Each direction in real space corresponds to a point in reciprocal space, and vice versa.[65,82,160,161]

This correspondence is a consequence of the mathematical relationship between the position and momentum of a particle. When we perform a Fourier transform on a function describing the spatial distribution of atoms in a crystal, the transform represents the crystal's diffraction pattern in reciprocal space. In such a diffraction pattern, the positions of points correspond to the spatial frequencies of the atomic arrangement in the crystal represented in terms of wavevector k of the reciprocal space (or the k space).

The de Broglie equation gives the wavelength of electrons as:[162,163]

$$\lambda = \frac{h}{(2 * m_e * E)^{\frac{1}{2}}}$$

Where λ is the wavelength of incident waves, h is Planck's constant, m_e is the mass of an electron and E is the electron energy. From this equation, the electrons with energies in the range of 20-200 eV would contribute to wavelength in angstroms range which is a useful measure for the range of interatomic distances.[160] These electrons have lower kinetic energy and can be used to probe surfaces due to their sensitivity to surface effects. The LEED spectroscopy uses the diffraction of the electron waves from crystal structures due to the periodic arrangements of the atoms. The diffraction patterns are representatives of constructive interference of scattered waves from the periodic placement of atoms. LEED can be considered as the 2D planar representation of a 3D reciprocal space. Braggs's law gives the conditions for constructive interference of EM waves:[164]

$$n\lambda = 2d * sin\theta$$

Here n is an integer number, d is the interatomic spacing, and θ is the angle of incidence.

In the k space, this can be represented in the vector representation using the Laue condition as:[164]

$$k - k' = \frac{2\pi}{d} * n$$

Here k is the incident wave vector, k' is the scattered wave vector, n is the number of atoms and the term (2π/d) represents the reciprocal lattice vector. When multiple atoms in a crystal satisfy this condition, bright diffraction patterns can be observed on the screen due to the collective constructive interferences of the low-energy electrons incident on the atoms. The same condition can be represented under Fourier transformation as below linking the real and reciprocal space:[82,162]

$$e^{i(k-k')*R} = 1$$

Here the term (k-k') is the reciprocal lattice vector (K), and R is the basis vector of the lattice.

2. Instrumentation

Considering the mean free path of an electron, the LEED analysis is carried out in a vacuum so that they can interact with the surface of the matter and travel the required distances for signal acquisition. The electrons used in LEED are low-energy electron beams in the range of 5-500 eV. A filament is used to generate the electron beam. The beam energy will determine the beam diameter and the coherence length. These are important parameters as they help determine the diffraction pattern as an ensemble of the domains

illuminated by the electron beam. Four different concentric grids pass the backscattered electrons signal.

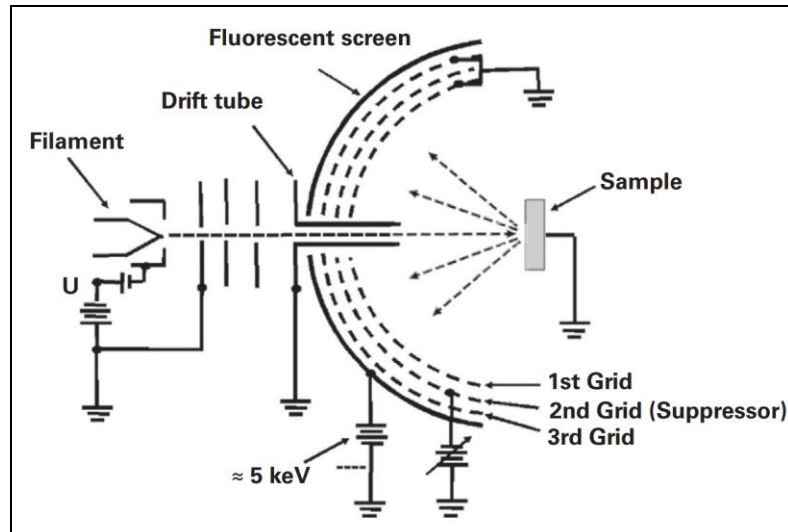

Figure 3.7. Simplified sketch of LEED instrumentation.[160]

The sample is grounded along with the first and the last grid. The middle two grids are coupled at a negative voltage. The grounded grids help preserve the signal from the sample while eliminating stray noise signals. The negatively charged grids are at a potential only slightly below the electron beam energy. These help pass only the quasi-elastically scattered electrons and fall on the phosphorescence screen creating a diffraction pattern. A camera captures this pattern and can be further analyzed in a computer system.

3.2.6. Electrical Characterization

1. Theory

For materials in electronics applications, the characterization of electrical properties is significant. It gives information about the material resistivity, contact resistance, material uniformity, carrier mobility, and carrier concentration. The four-probe

measurement setup can do this with a simple setup- two voltage-sensitive probes and two current-sensitive probes are used to get the material's resistivity using Ohm’s law. With negligible contact resistance and probe material resistance, the resistance of the sample under test is simply the ratio of the applied voltage to the measured current.[165]

$$R_{total} = R_{contact} + R_{probe} + R_{material}$$

$$R_{total} = V/I$$

2. Instrumentation

The material resistivity depends on internal factors like material composition, doping, and environmental degradation. So the probes are set in an inert environment like nitrogen where the material wouldn’t degrade due to oxidation. The probes with sharp tips are used to make contact with the sample by placing them at equally spaced points. A known voltage difference is applied across the inner two probes and the outer two probes measure the current conducted by the material. Using four probes instead of two gives the added advantage of eliminating the contact resistance and the resistance of the probe material. This method is also called Kelvin sensing.[166]

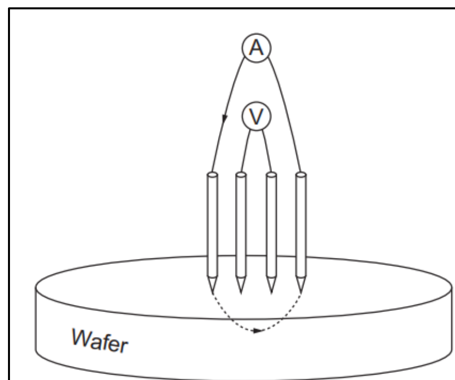

Figure 3.8. Four probes sensing on a sample.[165]

Chapter.4. UHV chamber and two-step growth of $MoTe_2$

4.1. Growth chamber

The UHV chamber which is used to grow TMDs is described in detail below. The turbomolecular pump and a backing rough pump create an ultra-high vacuum in the system. The base pressure is in the order of 1E-8 torr to 5E-9 torr. This is important for e-beam evaporation to prevent arcing and also to make a clean growth environment for the materials. The e-beam evaporation is used for Mo evaporation for $MoTe_2$ and $MoSe_2$. In the first iteration of chamber fabrication, the two Knudsen cells and two e-beam evaporators are loaded on two 6" rings. Each Knudsen cell has one quartz crystal microbalance (QCM) that measures the evaporation rate at the cell. A second QCM is used to calibrate the evaporation at the heater position with respect to the evaporation at the evaporation cell of the material. Because of the two separate evaporator rings the calibration can only be done for one combination of the evaporators at a time.

4.1.1. Electron beam (e-beam) evaporator

The transition metals have a high melting point and simpler thermal evaporation is not the best way to evaporate them. We use an e-beam evaporator (McAllister) to evaporate Mo or Ta.

It has a thoriated tungsten filament that can be heated by passing current through the power supply. The radiated heat is not enough to evaporate the Mo evaporant rod. To overcome this, the power supply can apply a high voltage in the range of 1060 V that accelerates the evaporation. The applied voltage attracts the electrons radiated from the filament and this bombardment of electrons on the evaporant rod causes the evaporation of atoms from the evaporant. The copper housing surrounding the evaporant and filament assembly is cooled by water which is supplied through a chiller.

The evaporant rod is modified from a single straight wire to increase the flux of transition metal during the growth. One variation uses three 0.5 mm diameter Mo wires spotwelded together and the other uses a combination of 0.5 mm and 0.75 mm diameter Mo wires spotwelded together. This method is recommended as it is easier to evaporate material from such a combination compared to using a single thick evaporant rod. The increased surface area of the combination assists in higher flux transmission. At the onset of the evaporation process, the combination rod melts at the tip to form a ball of molten material and consumes the evaporant as the evaporation duration increases. This ensures uniform evaporation which is a desired growth parameter.

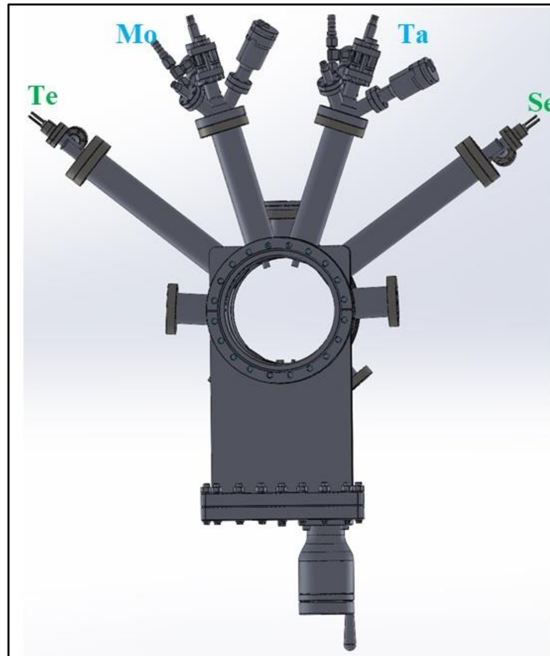

Figure 4.1. Transition metal e-beam evaporators and chalcogen Knudsen cells in growth chamber SolidWorks drawing.

4.1.2. Knudsen cell

Chalcogens have a relatively lower melting point. Such an effusion cell based on thermal evaporation can evaporate chalcogens like Se and Te. The chalcogen source shots or pellets are filled in a tungsten boat with a small orifice. The crucible boat is mounted on the current-carrying filament rods. A thermocouple is inserted in the boat to measure the temperature during evaporation. The Knudsen cell head has a quartz crystal connected to the quartz crystal microbalance (QCM) monitor. It measures the evaporation flux rate from the Knudsen cell and the e-beam evaporator. The power to the evaporators is adjusted based on the evaporation rate determined for the growth.

4.1.3. Sample heater

The heater filament is a thoriated tungsten wire shaped into an "M" shape. The ends are spotwelded to two tungsten pads that connects the current carrying leads to the filament. The filament is placed in a tungsten shell and is electrically isolated from the rest of the assembly with ceramic washers and spacers. The top plate has a substrate holding pocket made with tantalum foils. The K-type thermocouple is welded on the top plate. The top plate also has a high-voltage cable connected. When the current is passed through the filament, it heats up and the electrons can overcome the work function of the material to create an electron cloud around the hot filament. These electrons are accelerated toward the top plate that holds the substrate by applying a high voltage. For heating the filament in a controlled way, the high voltage is limited to a range of 200V. This avoids the creation of undesired arcing in the chamber.

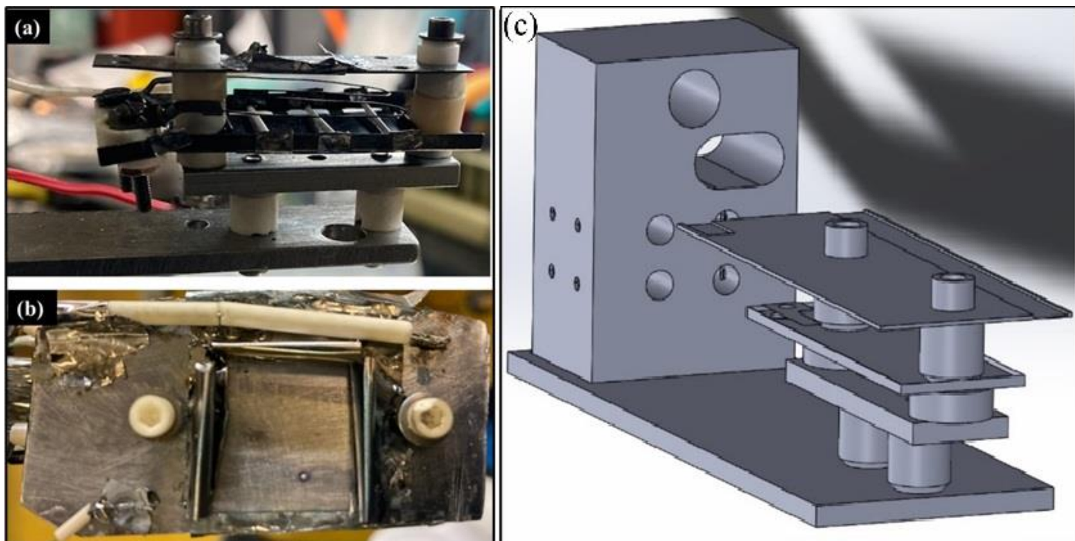

Figure 4.2. Heater assembly photo (a) side view and (b) top view; (c) SolidWorks drawing of the heater assembly and the wire routing aluminum block.

An aluminum block is used to route the electrical and thermal connections on the heater from the manipulator arm connectors. The block is designed with hollow tubes in which ceramic guiding tubes are inserted. Screw holes are drilled to fix the ceramic tubing. This block sits on a base plate that holds the rest of the assembly. The heater can be rotated 180° without tangling of the wires. These channels also help prevent undesirable electrical shortcuts and help with easier routing of wires to the expected location at the heater assembly. The sample can heat up to 700 °C on the heater.

To measure the sample temperature, a K-type thermocouple is used. This temperature-measuring device consists of two different conductors (usually metal alloys) that are connected at one end, forming a junction. When this junction is heated or cooled, it generates a voltage that can be measured and interpreted to determine the temperature. The principle underlying the operation of a thermocouple is known as the Seebeck effect.

The selection of metals for the thermocouple wires is crucial, as it determines the temperature range, sensitivity, and accuracy of the thermocouple. Different combinations of metals result in different types of thermocouples, such as K-type, J-type, T-type, etc. Each type of thermocouple has its own temperature range and characteristics. K-type thermocouples are widely used because they offer a relatively wide temperature range. They can measure temperatures from around -200°C (-328°F) up to approximately 1,370°C (2,498°F). K-type thermocouples are made by joining a wire of Chromel (an alloy of approximately 90% nickel and 10% chromium) with a wire of Alumel (an alloy of approximately 95% nickel, 2% manganese, 2% aluminum, and 1% silicon).

4.1.4. Quartz crystal microbalance

The evaporation fluxes are monitored using a quartz crystal microbalance. The core component is a disk of crystalline quartz, which is piezoelectric. This means it can generate an electric potential when subjected to mechanical stress and vice versa. When a voltage is applied to the electrodes on both sides of the quartz crystal plate, the piezoelectric effect causes the crystal to deform. In this case, the voltage induces shear deformation due to the inverse piezoelectric effect. The crystal is cut and oriented such that the applied voltage induces shear deformation rather than elongation or compression. This shear deformation is crucial for efficient operation. The quartz crystal plate has a natural acoustic resonance frequency of vibration when excited by an alternating current (AC) voltage. The large amplitude of oscillation at resonance corresponds to a large mechanical motion of the crystal plate.

When the evaporant atoms are adsorbed on the crystal, there is a change in the mass which induces a change in vibration frequency. The frequency shift is directly proportional to the mass change on the crystal's surface. By calibrating the QCM with known mass changes, it's possible to quantify the rate of evaporation.

The change in frequency with a change in mass is given mathematically by the Sauerbrey equation:

$$\Delta \mathbf{f} = -\frac{2f_0^2}{\mathbf{A}\sqrt{\rho_q \mu_q}}\,\Delta \mathbf{m}$$

Here Δf is the change in frequency, f_0 is the natural frequency of the crystal, A is the surface area of the electrode, ρ_q is the density, μ_q is the shear modulus of quartz crystal, and Δm is the change in mass.

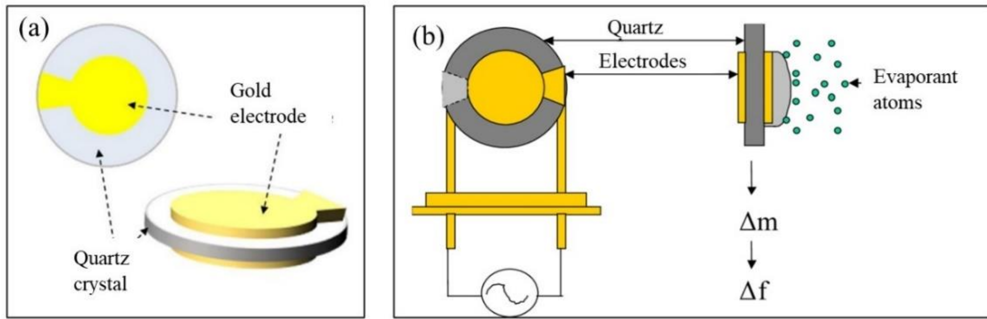

Figure 4.3. Quartz crystal with gold electrodes on top and bottom; (b) QCM monitoring for evaporation rate of atoms.[167]

As mentioned earlier, each of the Knudsen cell (Te and Se) has one such QCM. The chamber is also equipped with one so that the transition metal evaporation rate can be calibrated pre- and post-growth. The chalcogen evaporation rate can be monitored throughout the growth duration, but the transition metal evaporation needs to be calibrated for the desired rate from the emission current or the flux rate.

4.2. Substrate preparation

SiO_2: The silicon dioxide is grown on silicon crystals to make these wafers. The oxide thickness used in this study was ~300 nm. The substrates are cut into squares of size 2 cm * 2 cm. These are solvent-cleaned first using acetone, isopropyl alcohol, and deionized (DI) water. Next, the substrates are piranha cleaned in an H_2SO_4 and H_2O_2 (in ratio 3:1) mixture bath for 30 minutes. The last step is to clean these substrates with DI water and dry them with nitrogen.

GaN: The GaN samples are similarly cleaned in piranha etch solution, but only for 5 minutes, and then cleaned with DI water and dried with nitrogen.

Si: The SiO_2/Si substrate is solvent-cleaned before a buffered oxide etch (BOE) solution bath. The solution is a mixture of hydrofluoric acid and ammonium fluoride in water. This selectively etches the SiO_2 leaving behind a clean Si crystalline substrate. This method is used to study the growth quality contrast on amorphous SiO_2 and the crystalline underlying Si substrates.

4.3. Two-step growth of $MoTe_2$

The most common growth methods for these are CVD-based as discussed in the previous sections. Molybdenum oxide is a typical Mo precursor and the chalcogen powders or pellets can be used as chalcogen precursors. CVD growth occurs at temperatures as high as 600 °C to 900 °C, depending on the material grown.[125,168,169] Our method brings down the growth temperature significantly and does not require an additional annealing step as most conventional MBE or sputtering-based methods report.[136,170,171]

We found that the reported physical vapor deposition-like growth method can be successfully reproduced in our preliminary results. In this method, the substrate is heated to 240 °C and exposed to a high Te : Mo flux by heating the respective evaporators. The co-deposition proceeds for the required growth time and is followed by shutting the Mo evaporator and annealing the sample under an excess Te environment. The annealing is carried out at 400 °C for four minutes and ramped down to room temperature over the next six minutes. During annealing, the Te rate is higher than that during the co-deposition. This is important for avoiding chalcogen vacancies. The films are characterized by Raman spectroscopy, XPS, and electrical measurements.

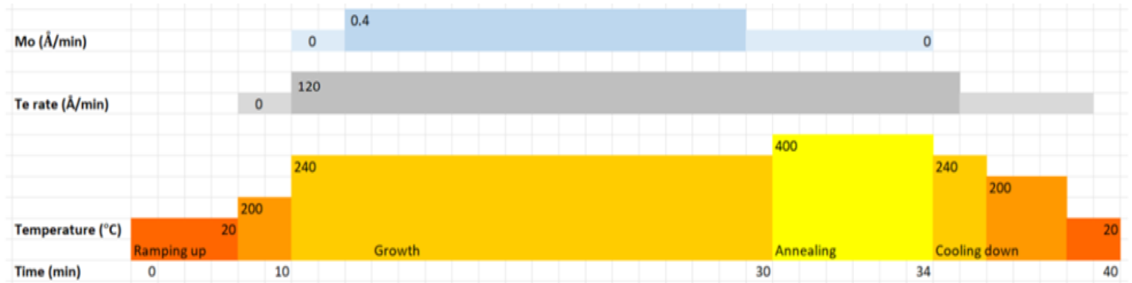

Figure 4.4. A timeline of $MoTe_2$ growth using the two-step method.

Samples of type A, B, and C are grown for 10, 20, and 30 minutes respectively by co-deposition of Mo and Te. All of these are then similarly annealed as previously explained. The respective characterization results represent the substrates on which the samples are grown.

The Raman spectroscopy of the $MoTe_2$ films prepared shows that the films prepared using the two-step method are 1T' or 2H or mixed-phase of 1T' and 2H $MoTe_2$. In the graphs shown below, the blue regions represent Te peaks, red represents 1T' peaks, and green represents the 2H $MoTe_2$ peaks. The two most prominent peaks on the samples A, B and C on SiO_2 or MoS_2 on SiO_2 are peaks around 160 (B_g) and 230 (E_{2g}) cm^{-1}. The B_g peak closely resembles the one in 1T' phase while the E_{2g} to the 2H phase of $MoTe_2$. The Raman spectroscopy on GaN is more challenging. This is possibly due to the lack of an oxide layer, but it requires further investigation and analysis. Raman spectra are shown below:

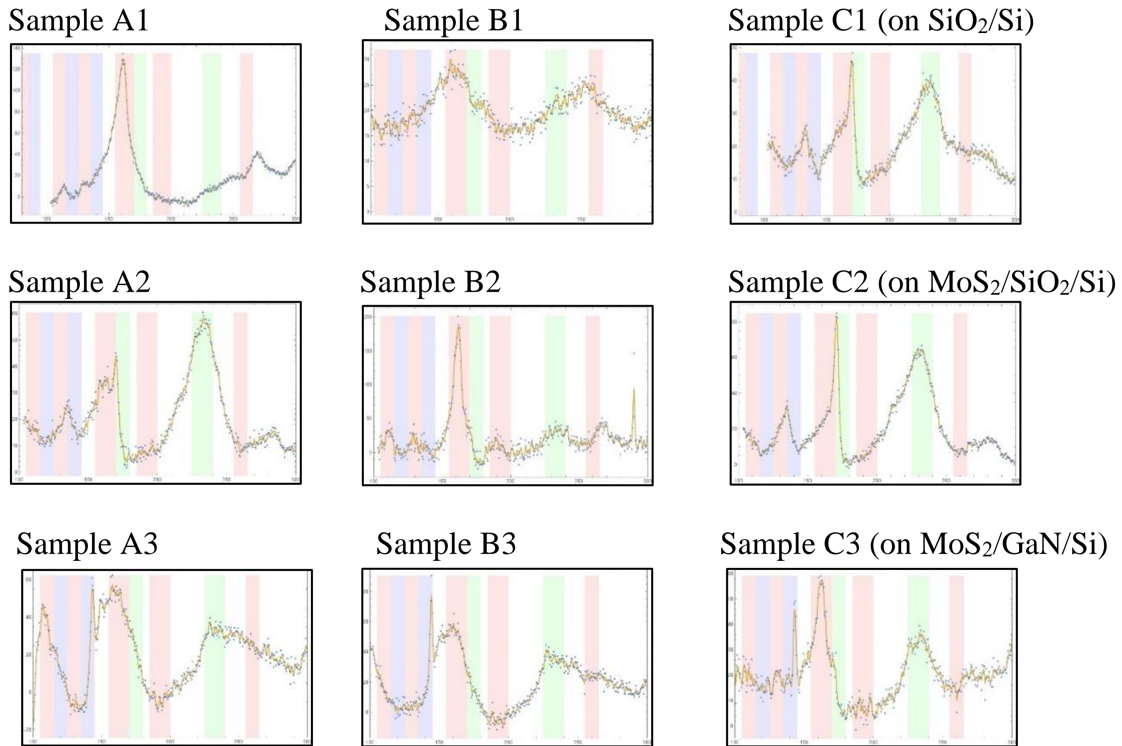

Figure 4.5. Sample A1, B1, and C1 represent the Raman spectra of $MoTe_2$ growth on SiO_2/Si substrates. Sample A2, B2, and C2 represent the Raman spectra of $MoTe_2$ growth on $MoS_2/SiO_2/Si$ substrates. Sample A3, B3, and C3 represent the Raman spectra of $MoTe_2$ growth on $MoS_2/GaN/Si$ substrates.

In the figure 4.5. I compare the Raman spectra quality for six samples. Samples A1, B1, and C1 are the $MoTe_2$ films grown on the 300 nm amorphous SiO_2/Si. The next three samples A2, B2, and C2 are grown to test the role of epitaxy. A thin MoS_2 is grown on the SiO_2/Si and this is used as the substrate for the subsequent $MoTe_2$ layers. The last three $MoTe_2$ samples A3, B3, and C3 are grown on a MoS_2/GaN/Si stack. For the three types tested, growth conditions are identical. The growth temperature is 240 °C in step one, and annealing is carried out at 400 °C in step two.

The electrical devices are designed to test the current-voltage (IV) characteristics. The $MoTe_2$ films are coated with polymethyl methacrylate (PMMA). They are next patterned with contact pads via electron beam lithography (EBL). The samples are then developed in MIBK and IPA. After developing step, the metal contacts are deposited on these patterns by evaporating 10 nm Y as adhesive metal and 200 nm gold. The excess gold is then lifted off using acetone and IPA. To bypass the issue of gate leakage, a rectangular region is isolated by a second patterning and developing steps followed by PECVD etching step.

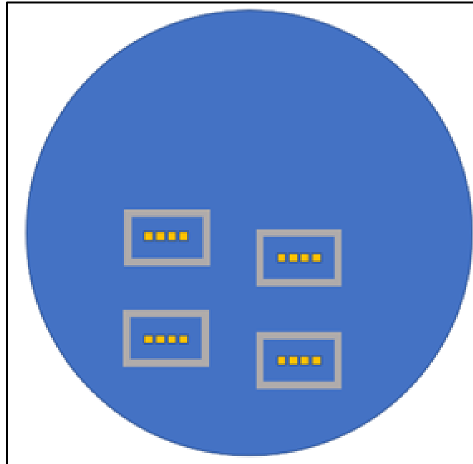

Figure 4.6. Four devices are fabricated on different areas of the sample to test the uniformity of film quality.

The four metal pads on each region form the contacts for a test device. The probes are landed on each of these pads. The central two are used as voltage leads and voltage is applied across K1 and GND. The two pads on the outside are used to measure the resultant current. The electrometers EM5 and EM6 are used to measure this current. A gate voltage can be applied across the silicon substrate.

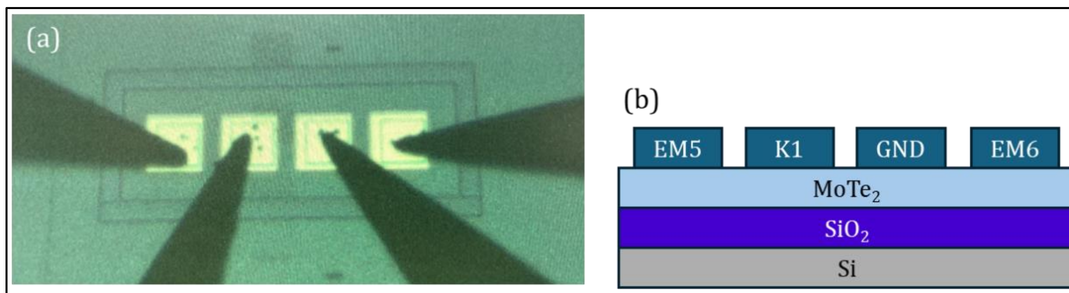

Figure 4.7. (a) 4 probe measurement setup. (b) Measurement stack and pads used to measure the electrical characteristics.

Current-voltage (I-V) characteristics- Overall, we see an increase in current with an increase in temperature for all tested gate voltage ranges for samples 2H $MoTe_2$ on

SiO_2/Si. Here T1 is 20 °C, T2 is 30 °C, T3 is 50 °C and T4 is 70 °C. While the current is constant for variation in gate voltage (V_{gate}).

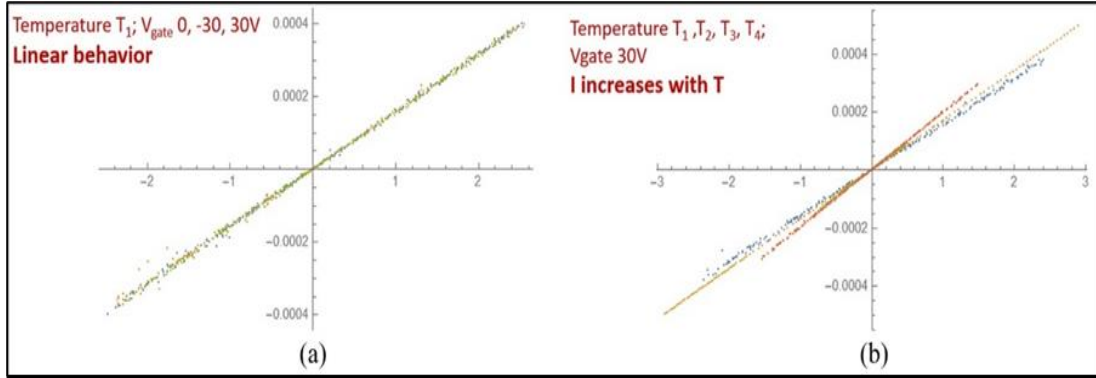

Figure 4.8. IV characteristics of 2H $MoTe_2$ on SiO_2/Si.

X-ray photoelectron spectroscopy (XPS)- The XPS data from previously investigated samples show the presence of $MoTe_2$ films. The Mo $3d_{5/2}$ and Te $3d_{5/2}$ are at 228.6 eV and 572.9 eV respectively.

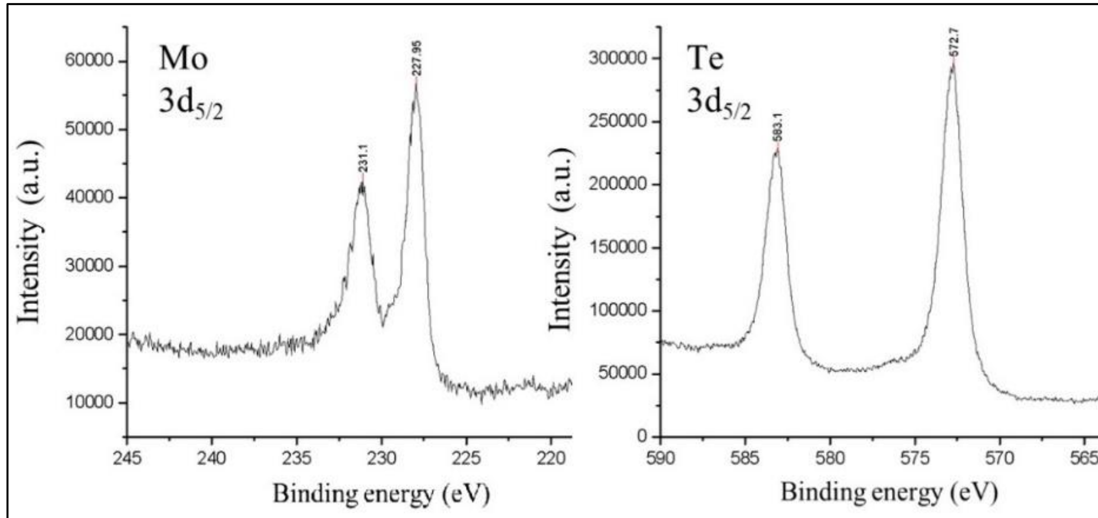

Figure 4.9. XPS of $MoTe_2$ on SiO_2/Si.

These preliminary results show that the growth is affected by the substrate significantly. The phase transition is likely to occur as growth time increases and could be an effect of an increase in the availability of adatoms. Additionally, the annealing temperature of 400 °C is identified as an important factor in forming the semiconducting 2H phase of $MoTe_2$. Next, some of the updates and the idea behind the updates to the chamber and the growth process are elaborated.

The $MoTe_2$ and $MoSe_2$ growths are to be based on the evaporation of the pure source elements in optimum pressure and temperature conditions in one section of the chamber and in the other section of the chamber, MoS_2 is to be grown using Mo filaments and H_2S as the gaseous precursor for S. These two sections of the chamber are separated by a gate valve. The substrate should travel along the length of the chamber and rotate to the required angles with the manipulator arm. The arm has electrical connections to heat the sample, measure the temperature, and apply high voltage for thermionic emission application. The $MoTe_2$ and $MoSe_2$ growth processes were designed to be lower growth temperature processes compared to the growth of MoS_2. If the Mo, Te, and Se evaporators are on the same ring, the arm would undergo minimum movement, prolonging the stability and lifespan of the equipment. Additionally, the QCM can be placed in one single position to calibrate the evaporation rates of all the different evaporators. The updated system is also designed to potentially add a RHEED system in the future for in-situ growth monitoring and be able to update the parameters as required in real-time.

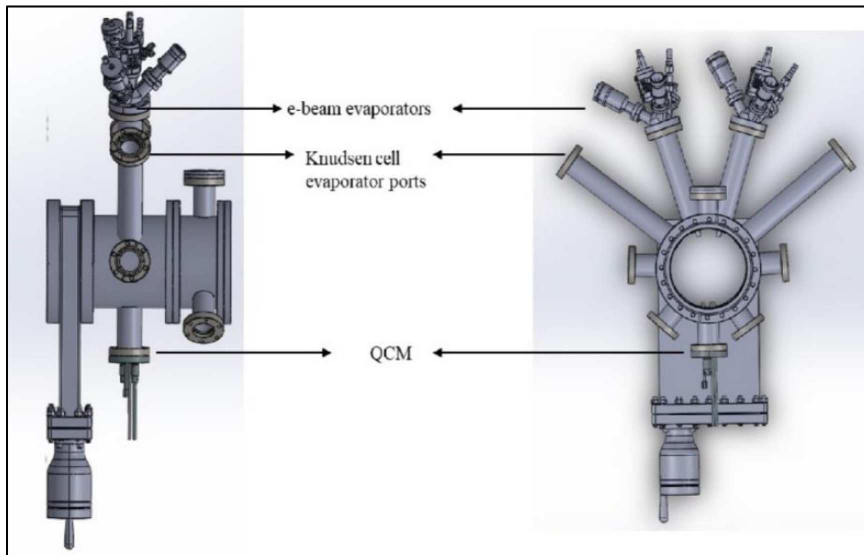

Figure 4.10. SolidWorks drawing of QCM and evaporators in the chamber.

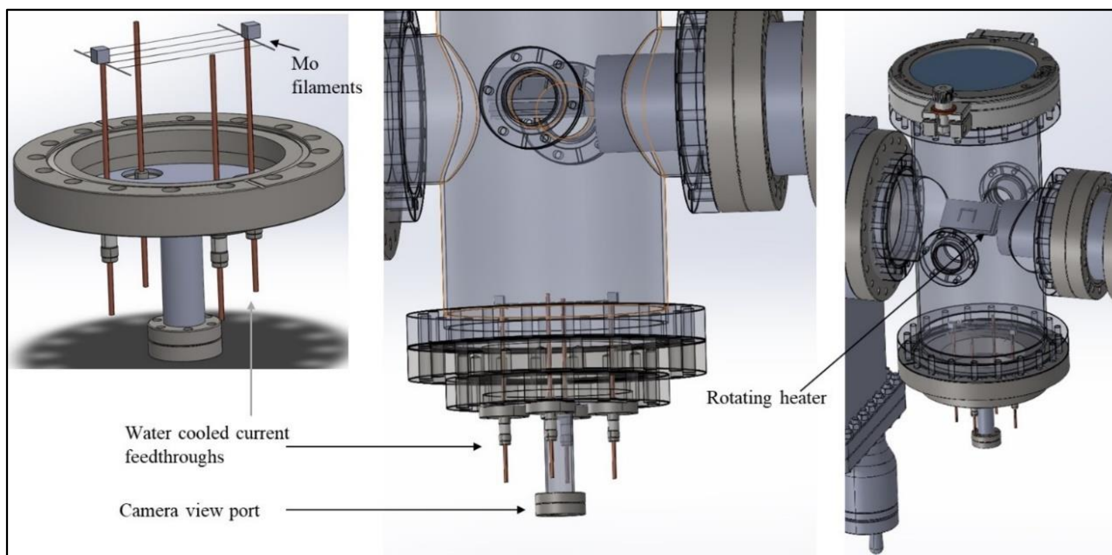

Figure 4.11. SolidWorks drawing of MoS_2 growth section of the chamber.

Camera

The growth of MoS_2 is based on the work of Almeida et. al.[137] They use a camera to monitor the layer-by-layer growth of MoS_2. A camera is mounted on a viewport that can look at the substrate and the Mo filament. The camera image contains hot Mo filament and its reflection on the silicon substrate. The camera captures a red-green-blue (RGB) image, and it is digitally transmitted to the computer in a hue-saturation-brightness (HSB) format. The hue parameter relates 8 bits to 256 hue intensity values. The highest values represent the first image captured by the camera of the reflection of the filament on the bare substrate. As the growth proceeds with sulfur precursor reacting with Mo and depositing MoS_2 on the substrate, the color of the substrate changes. This change is reflected in the subsequent images showing a drop in the contribution of the red hue.

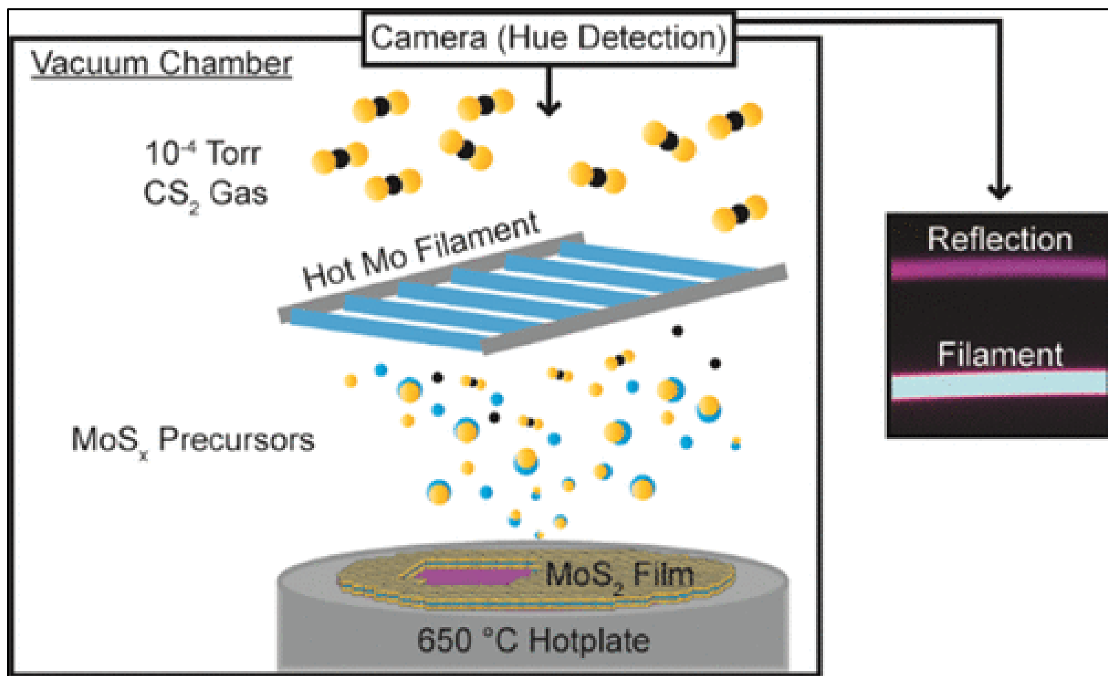

Figure 4.12. MoS_2 growth.[137]

Heater

The heater is redesigned with ceramic and refractory materials to improve the quality of heating and the robustness of the parts when subjected to a high flux of evaporants. The assembly is rebuilt to be supported by ceramic screws through the length which avoids electrical short-circuits from the top plate to the bottom ones. The heating filament is redesigned to have an increased surface area and thickness. The top plate is made with a tungsten plate to promote thermal conduction to the substrate. A sample holder pocket is created by spotwelding tantalum foil pieces in a square shape. Tantalum is relatively easy to spotweld onto the tungsten plate. The thermocouple is spotwelded close to the substrate position to measure the accurate temperature. The high-voltage cable is also spotwelded on the top plate. This heater can heat the sample to 700 °C.

4.4. MoS_2 growth

Due to the chamber design, the Mo filaments, camera, and leak valve are mounted on the bottom flange as shown in the drawing below. To grow MoS_2, the substrate is rotated 180° to face the precursors. The manipulator arm is positioned to capture the camera image to monitor the growth. The Mo filaments are resistively heated by passing a high current through them. The filaments heat to emit a yellow-whitish glow. At this stage, the sulfur precursor, H_2S gas, is passed into the chamber by opening the leak valve. The pressure of the system is maintained at around 1E-3 torr to create an environment conducive for the MoS_x species to nucleate on the substrate. The hue change is monitored to determine the thickness of the sample. The growth ends with a controlled ramp-down process.

The MoS_2 films are characterized by Raman spectroscopy and PL spectroscopy. The Raman spectrum below shows film uniformity by comparing spectrum at center, top-left (TL), top-right (TR), bottom-left (BL), and bottom-right (BR). The peak separation for MoS_2 is 19.5 which represents a monolayer film.[137] The peak at 520 cm^{-1} represents the Si substrate. PL peak is also provides additional evidence of monolayer MoS_2.[137]

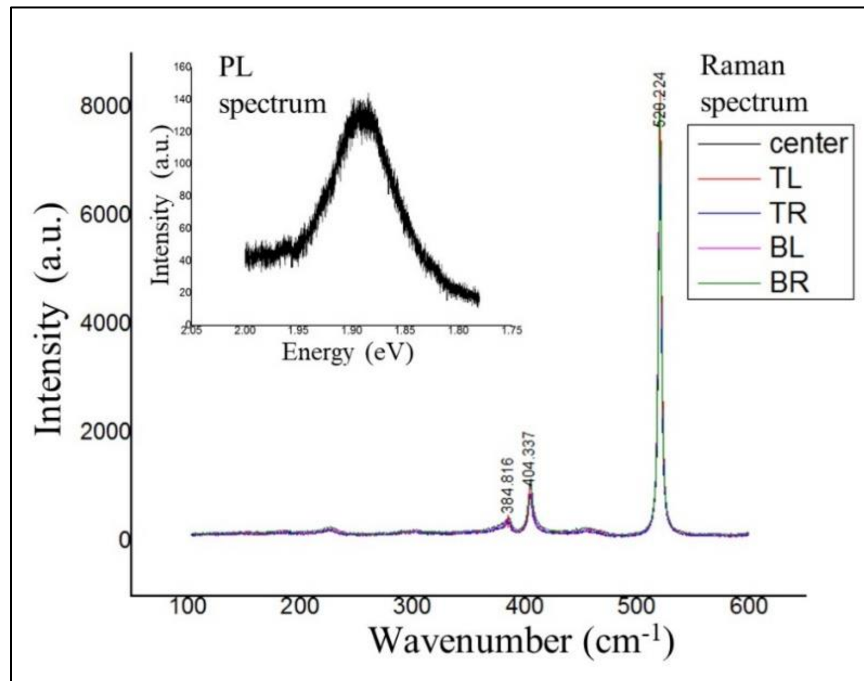

Figure 4.13. Raman and PL spectrum of MoS_2 on SiO_2/Si.

Complete chamber for a single step growth:

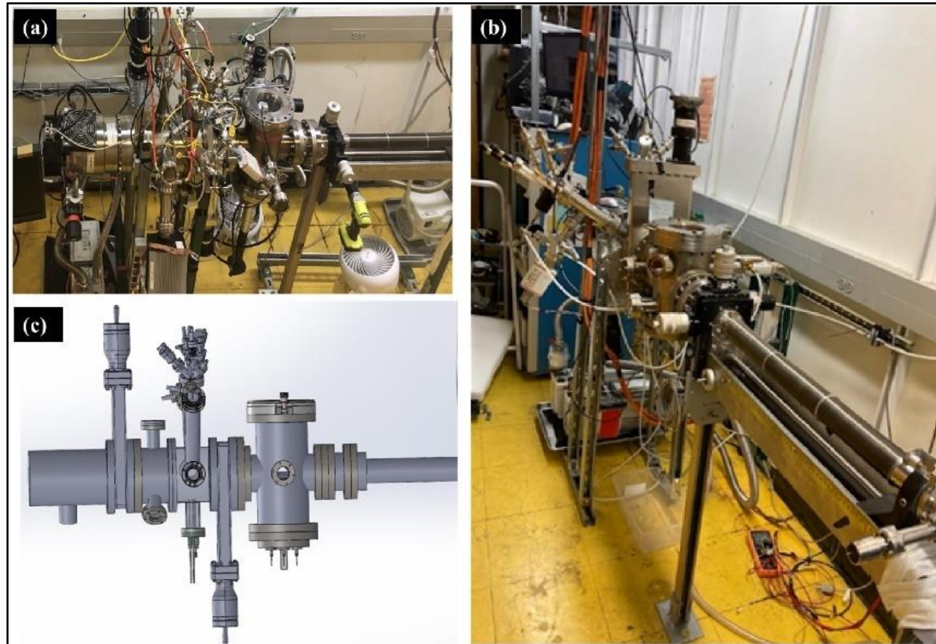

Figure 4.14. UHV growth chamber (a) top view photo; (b) front view photo; (c) side view SolidWorks drawing.

The single-step growth is proposed to occur at around 400 °C. The evaporant cells are heated to get a predetermined targeted flux ratio. At the end of the growth process, the supply of evaporants is shut and the sample is brought to room temperature in a single step.

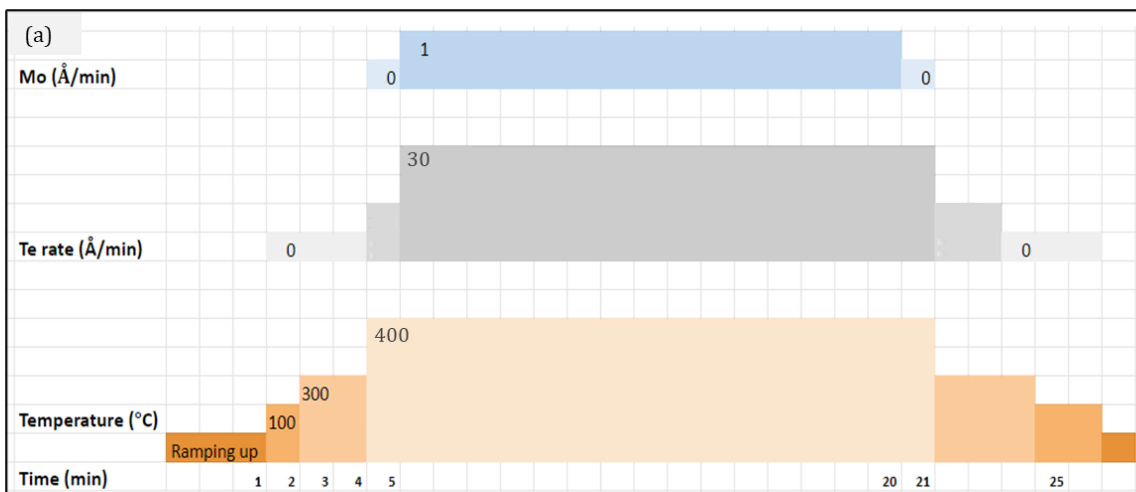

Figure 4.15. A timeline of single-step growth of $MoTe_2$.

Chapter.5. Single-step TMD growth

The following chapter contains excerpts from "**Rapid and Facile growth of High-Quality 2H-$MoTe_2$ Films on SiO_2 by means of an in-situ-grown MoS_2 Buffer Layer**" (In preparation)

5.1. Motivation

Two-dimensional (2D) Transition Metal Dichalcogenide (TMD) compounds are composed of a transition metal atom sandwiched between two chalcogen atoms, with each sandwich layer bonded to the adjacent ones via van der Walls (vdW) interactions. TMD materials can be semiconductors, semimetals, or topological insulators depending on their composition and the structural phase of the vdW material.[110,172,173]

While molybdenum sulfides and selenides are comparatively facile to grow and both widely studied, molybdenum tellurides require more attention to exploit the material for cutting-edge applications.[174,175] The small electronegativity difference between Mo and Te, makes the $MoTe_2$ layers prone to environmental degradation and relatively more difficult for controlled growth.[176] Molybdenum ditelluride ($MoTe_2$) can occur in three different phases- 2H, 1T', and 1Td, out of which the 2H is a stable semiconducting while 1T' is a stable semimetallic phase. The Td phase is a metastable phase that eventually transitions to 1T'.[177] The energy difference between the 2H and 1T' phases of $MoTe_2$ is only about 44meV.[178] The monolayers of 2H semiconducting phase of $MoTe_2$ exhibit a direct bandgap of 1eV and multilayers exhibit an indirect bandgap of 0.88eV.[179] This range of bandgap of the material is of interest for electronic and optoelectronic device applications.[180,181]

CVD, CVT, mechanical exfoliation, and MBE are the methods typically used to grow 2D $MoTe_2$.[99,109,125,132,168,170,182–187] The CVD or CVT processes use chemical precursors in synthesis and the mechanical exfoliation method makes use of the vdW interactions that help peel the materials that can then be transferred to a desired substrate. While conventional CVD, CVT, and mechanical exfoliation are more commonly used, vacuum-based growths offer a cleaner environment for synthesis and are a growing area of research. In this study, we present a phase-controlled growth mechanism of $MoTe_2$ in the UHV system using PVD-type growth. Our study offers insights into the role of the underlying substrate in the growth of subsequent layers and we develop a phase diagram for Mo-Te compound growth via this co-deposition in the UHV chamber.

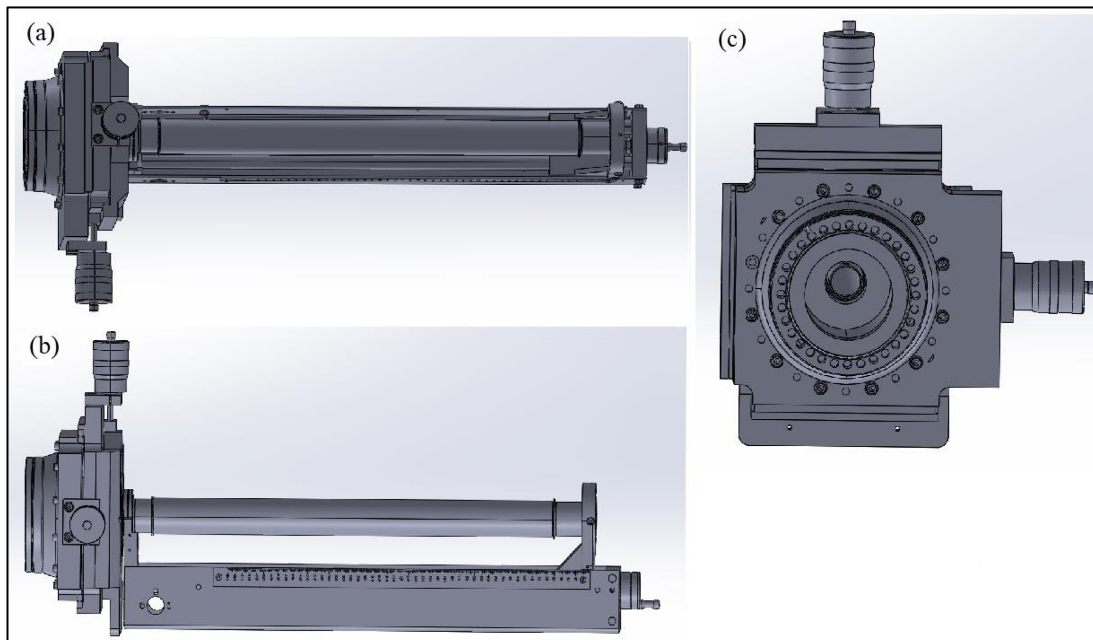

Figure 5.1. Manipulator arm (a) top view, (b) side view, and (c) front view.

While both the 1T' and the 2H phases can be used in electronic devices for their individual properties, the controlled growth of one phase is challenging due to the small energy difference between the two.[188] For controlled growth, the substrate temperature and relative fluxes of atoms determine the adsorption-desorption rates. This is why, although $MoTe_2$ can be grown at relatively lower temperatures in non-CVD processes, the cooldown is tailored to accommodate for adding more Te to compensate the deficient sites or evaporate excess Te for more crystalline forms of films. This most commonly involves an annealing step under specific conditions which makes the growth time much longer. The mechanisms of phase transformation during growth offer interesting insights for MBE-type system which differs from CVD mechanisms. The 1T' phase propensity in CVD is due to Te deficiencies and in the case of MBE, it is proposed to be due to charge transfer.[168,169,188] Post-growth transformations can occur through other stimuli, but the energy barrier that needs to be overcome in that case is larger. Therefore, optimum growth conditions are the best route to phase-controlled synthesis.[132,172,189–191] From the previously studied phase diagrams, we see that in the narrow range of flux and temperature variations where computationally, a crisp phase boundary was anticipated, experimentally, the occurrence of mixed-phase is found to be common.[114,169] So the challenge that we attempt to address here is find optimum growth conditions a rapid and, one-step low-temperature growth of $MoTe_2$ with moderate Te to Mo abundance and bypass the need for a prolonged and, controlled cooldown on a SiO_2/Si substrate with and without a buffer layer. The buffer layer of MoS_2 has a significant effect on the phase of the $MoTe_2$ grown subsequently. In the phase diagram developed in this study, we find that both 1T'- and 2H-$MoTe_2$ can be

grown on bare SiO_2/Si substrate. When a thin MoS_2 buffer layer is introduced, only 2H-$MoTe_2$ is formed under the conditions involved in this study.

5.2. Experiments

The UHV chamber used has a base pressure of 1E-8 torr. It is divided into two sections: part 1- $MoTe_2$ growth chamber; and part 2- MoS_2 growth chamber. The substrate is loaded on a heater arm that can transit between the two sections of the chamber without breaking the vacuum.

1. MoS_2 growth:

A SiO_2/Si substrate is cleaned by piranha etching, then loaded on the heater, and transferred to the growth chamber. The Mo filaments are heated in the presence of H_2S gas. The activated H_2S reacts with Mo to deposit the MoS_2 layers on the heated substrate. The completion of the growth is determined by camera metrology explained by Almeida et. al.[192] For this study, we grow thin MoS_2 films (~2 layers) as the underlying layer for the Mo-Te deposition.

2. $MoTe_2$ growth:

An e-beam evaporator (McAllister) is used to generate Mo flux and a Knudsen cell is used for Te flux. Once the substrate reaches growth temperature, Mo and Te are co-deposited on the substrate for growth duration. The duration of growth is determined by calibrating the Mo flux rate corresponding to the required number of layers. The co-deposition process is followed by a cooldown process. During the cooldown, a temperature ramp is set to cool the substrate to 350 °C in 5 minutes followed by subsequent complete

shutting off the heater in the next 5 minutes. The Te cell is on only for the first 2 minutes of the cooldown and then is shut off completely during the rest of the process.

Batch A is the $MoTe_2$ grown on bare SiO_2/Si substrates and batch B is $MoTe_2$ on MoS_2/SiO_2/Si. The films are characterized by Raman and PL spectroscopy, TEM, and SEM. These methodologies help understand the factors leading to a phase-controlled growth, quality, and uniformity of the films and help enlighten the next steps in materials research.

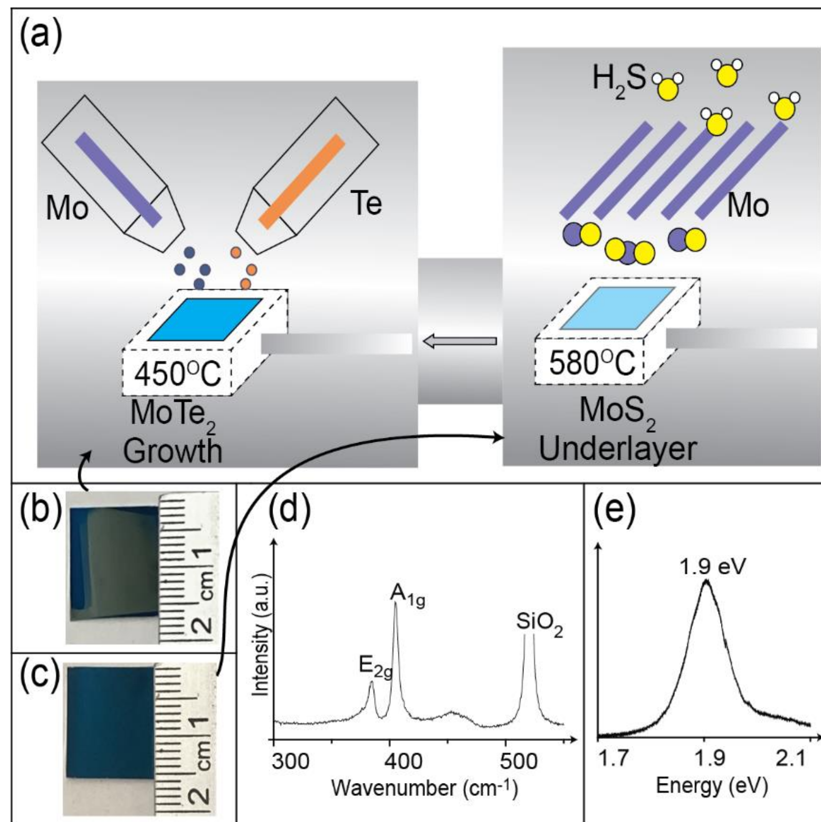

Figure 5.2. Chamber setup with $MoTe_2$ (left) and MoS_2 (right) growth regions. The substrate is placed on a heater arm that moves the sample between two growth regions. (b), (c) Optical images of multilayer $MoTe_2$ and monolayer MoS_2 growth on SiO_2/Si respectively. (d), (e) Raman and photoluminescence spectrum of MoS_2 underlayer grown on SiO_2/Si respectively.

5.3. Characterization

5.3.1. Raman

Raman spectroscopy measurements are carried out using HORIBA LabRAM with a 532 nm laser source. The $MoTe_2$ films are allowed to cool down to room temperature and then taken out of the vacuum chamber for the Raman spectroscopy measurements. The substrates are exposed to air in the process of carrying it to the spectroscopy setup.

1. 2H $MoTe_2$: The major Raman vibration modes for the 2H $MoTe_2$ phase correlate to the ones found in the literature. We find A_{1g} peak in the range of 167-170.3 cm^{-1} and, E^1_{2g} peak at 238.5-229.1 cm^{-1}
2. 1T' $MoTe_2$: The Raman peaks for 1T' $MoTe_2$ are observed at 160 cm^{-1}, which is the Ag vibration mode of this phase of $MoTe_2$.
3. MoS_2: The peak separation of E_{2g} band and A_{1g} band is observed to be ~20 cm^{-1} in the case of bare MoS_2 on SiO_2 and MoS_2 that occurs as the underlying layer for $MoTe_2$ growth. Interestingly, however, we observe the shift in the underlying MoS_2 layer as E_{2g} peak is at 400.36 cm^{-1} from 405.36 cm^{-1}, and the A1g peak is at 380.32 cm^{-1} from 385.34 cm^{-1}. A PL peak is observed on bare MoS_2 on the SiO_2 substrate at around 1.9 eV. This peak is unaffected by the subsequent growth of $MoTe_2$ under different growth conditions.

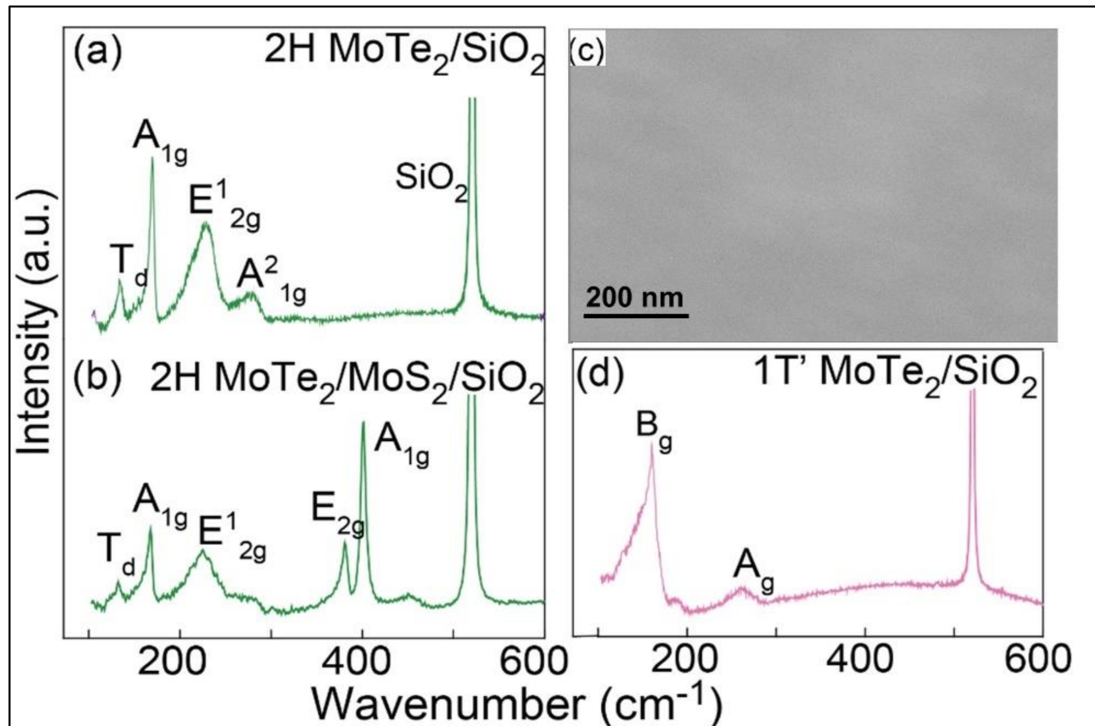

Figure 5.3. Raman spectrum of 2H $MoTe_2$ grown on SiO_2 substrate; (b) Ramana spectrum of 2H $MoTe_2$ grown on SiO_2 substrate with underlying MoS_2 layer; (c) SEM images of planar films; (d) Raman spectrum of 1T' $MoTe_2$ grown on SiO_2 substrate.

5.3.2. TEM

The $MoTe_2/MoS_2/SiO_2$ crosssection is investigated with TEM to check the structural integrity of the laminar structure. The lamellar sample is cut from the substrate using a focused ion beam (FIB) milling technique and loaded on a TEM grid.

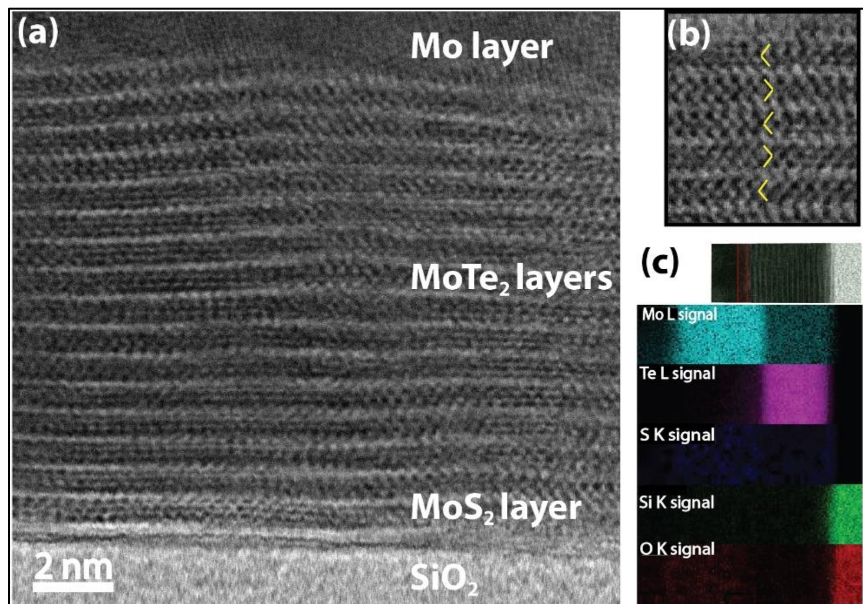

Figure 5.4. TEM image of layered $MoTe_2$ grown on $MoS_2/SiO_2/Si$ substrate. (b) Zoomed-in region of the TEM image shows atomic arrangements in the layered structure. (c) EDS mapping of a section of the TEM lamina.

5.3.3. SEM

The films are uniform and planar. At the maximum magnification, we do not find any features on the planar surface of the films, which implies the surface of the film is clean and uniform.

5.4. Results

We show the growth regime for 2H $MoTe_2$ on two different substrates. One is amorphous SiO_2 on Si, and the other one has a MoS_2 thin layer over the SiO_2/Si. The underlying MoS_2 helps in the epitaxial growth of the $MoTe_2$ on subsequent layers. We see the effects of this on the sections of the phase diagram of as-grown $MoTe_2$ films where 1T' phase was preferred on the amorphous substrate; we observe either a 2H phase or the absence of $MoTe_2$ peaks. This implies that the underlying epitaxial layers set a preference for making one phase of $MoTe_2$ over the other. Thus in the ranges of parameters in this study, we only get 2H $MoTe_2$ or no $MoTe_2$ on the MoS_2/SiO_2/Si substrates. We can attribute the absence to the Te flux or the temperature being unconducive to making a 2H phase $MoTe_2$ film.

We obtain a phase diagram for the described growth process by varying the growth conditions of substrate temperature and relative fluxes of Mo and Te. By virtue of the geometry of the growth chamber, we find a variation in the tellurium rate at the source of the Te to the substrate mounted on the heater. A calibration process is carried out to establish the flux rate for tellurium while keeping the Mo flux from the ebeam evaporator constant. The approximate rate of $MoTe_2$ deposition is calculated to be a monolayer per minute. The phase diagram is made by using thicker samples that are nearly 15 layers.

From the phase diagram, we can see that the $MoTe_2$ grown on the SiO_2 substrate is 1T' type in case of low Te flux. The 2H phase starts to take form when the substrate temperature ranges from 400 °C to 520 °C for Te flux rate increases to 0.1 Å/s. The quality of 2H $MoTe_2$ increases with flux and temperature to the optimum range and then declines for the highest temperature and flux values. The phase changes back to 1T' at high Te flux at low temperatures.

The underlying layer has a clear impact on the $MoTe_2$ layers grown on top of it. The phase diagram clearly shows the 2H phase of $MoTe_2$ on the SiO_2 substrate with underlying MoS_2 thin film. There is no 1T' $MoTe_2$ observed for the conditions in this study.

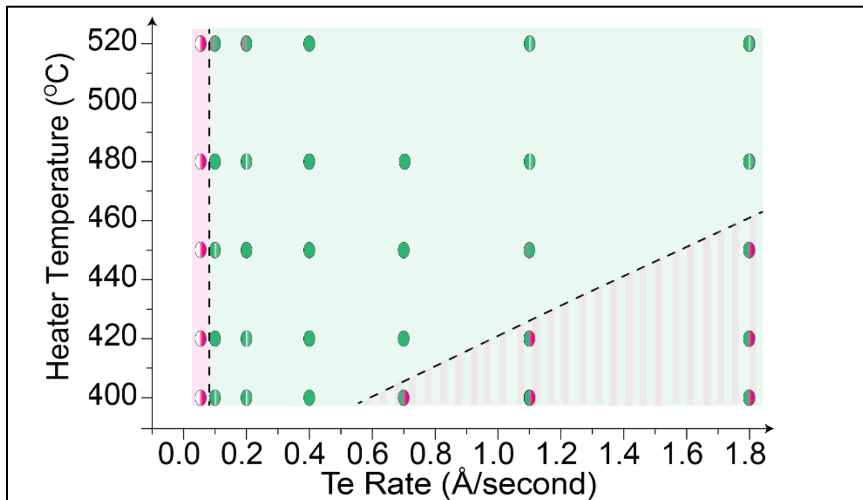

Figure 5.5. Phase diagram of Mo-Te growth via co-deposition method. The green color represents 2H phase of $MoTe_2$ and the red color represents the 1T' phase of $MoTe_2$.

The circles represent growth temperature and Te flux rate. The right half of the circles denotes the phase grown on SiO_2/Si substrate and the left half represents the phase grown on MoS_2/SiO_2/Si substrate.

5.5. Summary

The growth method is a versatile process to growth good quality $MoTe_2$ on a range of substrates. The phase diagram developed offers more insights into the preferential growth at different conditions. Both 1T' and 2H $MoTe_2$ can be successfully grown on SiO_2/Si. With the addition of an MoS_2 underlayer, the 2H phase is preferentially grown over 1T' for most of the parameters under test. The layered structure is verified further with cross-sectional TEM analysis. This fast and facile growth process can be adopted for further applications.

Chapter.6. Implications, Outcomes, and Summary

As described in the preceding chapters, the growth in the built UHV chamber is a versatile process implemented to grow other materials and heterostructures. Some of the projects related to this and the scope for future work are discussed in this chapter.

Other projects

1. $MoSe_2$ growth: the co-deposition method can be extended to growing $MoSe_2$ with some modifications. The growth temperature for $MoSe_2$ is 320 °C as the Se evaporates at lower temperatures than Te. The Mo and Se are deposited on the hot substrate for 10 minutes. The Mo supply is shut followed by a rapid ramp down of the Se supply and the substrate is brought to room temperature. The Raman spectroscopy characterization shows sharp and intense peaks of $MoSe_2$ implying a superior quality material formation.[100] The E_{1g} peak is at 168 cm^{-1}, A_{1g} mode is observed at 239.8 cm^{-1} and the E^1_{2g} peak at 286 cm^{-1}.[193,194]

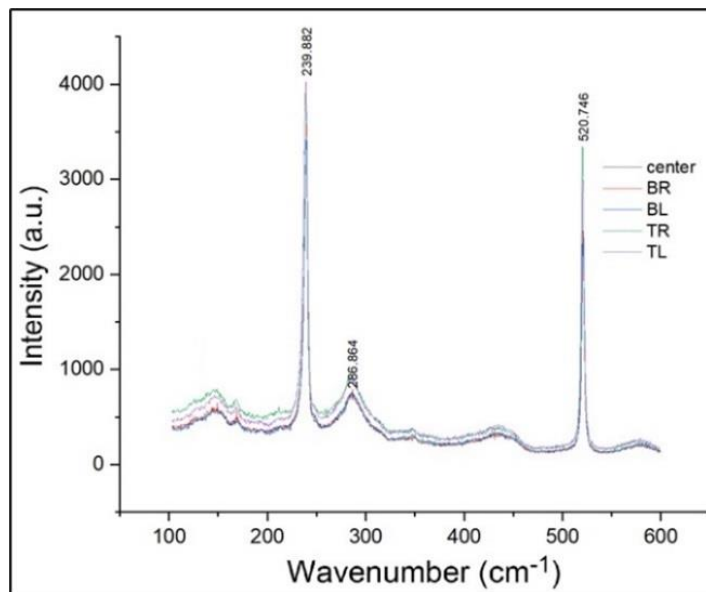

Figure 6.5. Raman spectrum of $MoSe_2$ grown on SiO_2/Si

2. $MoS_2/MoTe_2/MoS_2/SiO_2/Si$: a MoS_2 passivation layer can be grown on $MoTe_2/MoS_2/SiO_2/Si$ structure without damaging the $MoTe_2$ layer. This has been shown using Raman spectra below. As a proof of concept, this paves the way to make more complex heterostructures for future work.

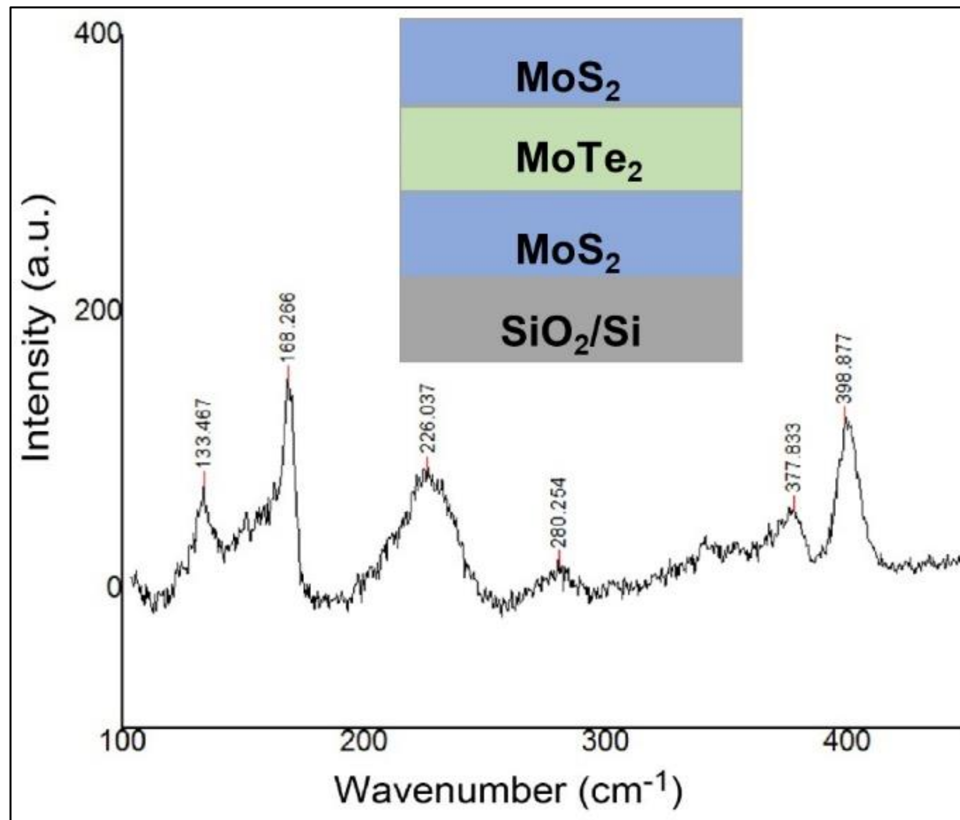

Figure 6.6. Raman spectrum of heterostructure: $MoS_2/MoTe_2/MoS_2/SiO_2/Si$.

3. LEED: As LEED is related to electron diffraction from the substrate, a thin $MoTe_2$ is grown on the $MoS_2/GaN/Si$ substrate. Using the LEED (OCI LEED system) analysis of the sample shows a diffraction pattern on the MoS_2 and $MoTe_2$ regions of the sample. Due to the small difference in lattice constant between MoS_2 and $MoTe_2$ the diffraction pattern requires further analysis. The $MoTe_2$ thin layer is prone to oxidation and such degradation affects the LEED quality negatively. We

have successfully developed a process to preserve the $MoTe_2$ by evaporating a thick Se layer on top that can be evaporated to remove the Se while preserving the underlying $MoTe_2$. Future work will involve developing a sample heater within the LEED chamber so that the Se coated sample can be transferred from the growth chamber to the LEED analysis chamber.

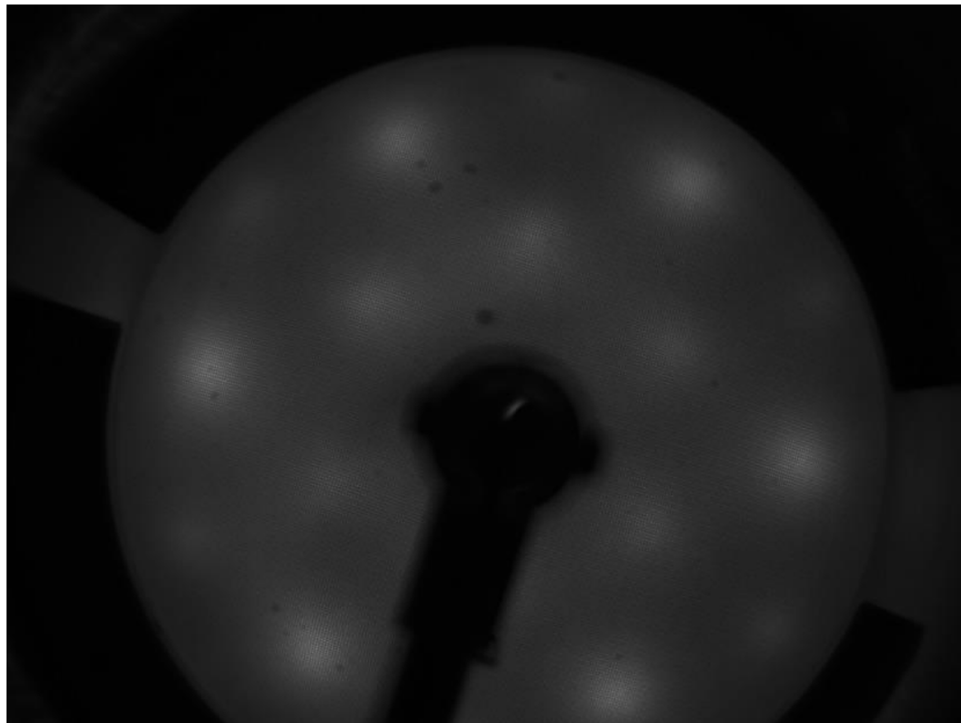

Figure 6.7. LEED image of $MoTe_2/MoS_2/GaN$.

4. Cross-sectional TEM: The cross-sectional TEM imaging helps provide additional evidence of layered growth of the $MoTe_2$ on the substrate. Despite a rapid growth of nearly one layer per minute, the multilayer samples grow almost epitaxially. The Fourier transform of the image shows the periodic variation of the atoms in different layers.

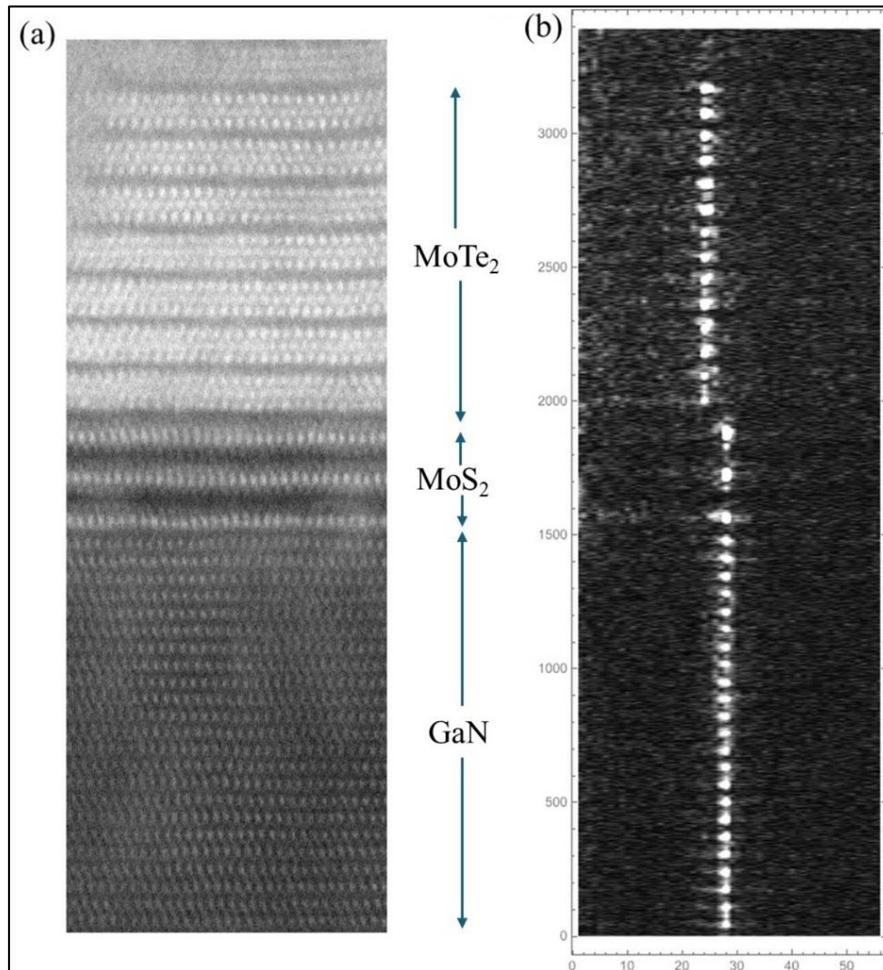

Figure 6.8. Cross-sectional TEM image and (b) TEM Fourier transform of the $MoTe_2/MoS_2/GaN$

In conclusion, we have shown that TMD materials based on Mo, Te, Se, and S can be grown in a broad range of parameter variation. The phase diagram developed in this work adds to the knowledge of materials growth in vacuum conditions at low temperatures and flux ratios. This method can be used for controlled, fast, and reliable growth of pure phase TMD materials and their heterostructures. Further work is required to advance the proof of concepts mentioned in this chapter for advanced applications.

References

1. Shalf, J. The future of computing beyond Moore's Law. *Philosophical Transactions of the Royal Society A: Mathematical, Physical and Engineering Sciences* **378**, 20190061 (2020).
2. Ohring, M. & Kasprzak, L. Chapter 12 - Future Directions and Reliability Issues. in *Reliability and Failure of Electronic Materials and Devices (Second Edition)* (eds. Ohring, M. & Kasprzak, L.) 665–700 (Academic Press, Boston, 2015). doi:https://doi.org/10.1016/B978-0-12-088574-9.00012-4.
3. Zhang, Q., Liu, C. & Zhou, P. 2D materials readiness for the transistor performance breakthrough. *iScience* **26**, 106673 (2023).
4. Lin, Y. *et al.* Scaling aligned carbon nanotube transistors to a sub-10 nm node. *Nat Electron* **6**, 506–515 (2023).
5. Kanungo, S., Ahmad, G., Sahatiya, P., Mukhopadhyay, A. & Chattopadhyay, S. 2D materials-based nanoscale tunneling field effect transistors: current developments and future prospects. *NPJ 2D Mater Appl* **6**, 83 (2022).
6. Pal, A. *et al.* Quantum-Engineered Devices Based on 2D Materials for Next-Generation Information Processing and Storage. *Advanced Materials* **35**, 2109894 (2023).
7. Lee, Y. *et al.* Spin-defect qubits in two-dimensional transition metal dichalcogenides operating at telecom wavelengths. *Nat Commun* **13**, 7501 (2022).
8. Schuman, C. D. *et al.* Opportunities for neuromorphic computing algorithms and applications. *Nat Comput Sci* **2**, 10–19 (2022).
9. Henke, K., Kenyon, G. T. & Migliori, B. Machine Learning in a Post Moore's Law World: Quantum vs. Neuromorphic Substrates. in *2020 IEEE Southwest Symposium on Image Analysis and Interpretation (SSIAI)* 74–77 (2020). doi:10.1109/SSIAI49293.2020.9094596.
10. Park, S. *et al.* Nonvolatile and Neuromorphic Memory Devices Using Interfacial Traps in Two-Dimensional WSe2/MoTe2 Stack Channel. *ACS Nano* **14**, 12064–12071 (2020).
11. Peper, F. The End of Moore's Law: Opportunities for Natural Computing? *New Gener Comput* **35**, 253–269 (2017).
12. Kwon, J. *et al.* Three-dimensional monolithic integration in flexible printed organic transistors. *Nat Commun* **10**, 54 (2019).
13. Liu, A. *et al.* The Roadmap of 2D Materials and Devices Toward Chips. *Nanomicro Lett* **16**, 119 (2024).

14. Nanomaterials pave the way for the next computing generation.

15. Lou, S. *et al.* Tunable growth of one-dimensional graphitic materials: graphene nanoribbons, carbon nanotubes, and nanoribbon/nanotube junctions. *Sci Rep* **13**, 4328 (2023).

16. Jiang, X.-F. *et al.* Recent Progress on Fabrications and Applications of Boron Nitride Nanomaterials: A Review. *J Mater Sci Technol* **31**, 589–598 (2015).

17. Ziegler, J. M. *et al.* Sensors Based Upon Nanowires, Nanotubes, and Nanoribbons: 2016–2020. *Anal Chem* **93**, 124–166 (2021).

18. Cotta, M. A. Quantum Dots and Their Applications: What Lies Ahead? *ACS Appl Nano Mater* **3**, 4920–4924 (2020).

19. García de Arquer, F. P. *et al.* Semiconductor quantum dots: Technological progress and future challenges. *Science (1979)* **373**, eaaz8541 (2024).

20. Lu, F., Wang, H., Zeng, M. & Fu, L. Infinite possibilities of ultrathin III-V semiconductors: Starting from synthesis. *iScience* **25**, 103835 (2022).

21. Gilbert, M. J. Topological electronics. *Commun Phys* **4**, 70 (2021).

22. Wang, P. *et al.* Dawn of nitride ferroelectric semiconductors: from materials to devices. *Semicond Sci Technol* **38**, 043002 (2023).

23. Yim, K. *et al.* Novel high-κ dielectrics for next-generation electronic devices screened by automated ab initio calculations. *NPG Asia Mater* **7**, e190–e190 (2015).

24. Kumar, J., Birla, S. & Agarwal, G. A review on effect of various high-k dielectric materials on the performance of FinFET device. *Mater Today Proc* **79**, 297–302 (2023).

25. Shaukat, R. A. *et al.* Organic semiconductor polymers: a carbazole-based novel tribopositive polymer for energy harvesting with high temperature stability. *J Mater Chem A Mater* **11**, 14800–14808 (2023).

26. Peng, Z., Chen, X., Fan, Y., Srolovitz, D. J. & Lei, D. Strain engineering of 2D semiconductors and graphene: from strain fields to band-structure tuning and photonic applications. *Light Sci Appl* **9**, 190 (2020).

27. Bernardi, M., Ataca, C., Palummo, M. & Grossman, J. C. Optical and Electronic Properties of Two-Dimensional Layered Materials. **6**, 479–493 (2017).

28. Sun, Y., Sun, M. & Xie, D. 5 - Graphene Electronic Devices. in *Graphene* (eds. Zhu, H., Xu, Z., Xie, D. & Fang, Y.) 103–155 (Academic Press, 2018). doi:https://doi.org/10.1016/B978-0-12-812651-6.00005-7.

29. 15 years of graphene electronics. *Nat Electron* **2**, 369 (2019).

30. Wang, Q. H., Kalantar-Zadeh, K., Kis, A., Coleman, J. N. & Strano, M. S. Electronics and optoelectronics of two-dimensional transition metal dichalcogenides. *Nat Nanotechnol* **7**, 699–712 (2012).

31. Chakraborty, S. K., Kundu, B., Nayak, B., Dash, S. P. & Sahoo, P. K. Challenges and opportunities in 2D heterostructures for electronic and optoelectronic devices. *iScience* **25**, 103942 (2022).

32. Molaei, M. J., Younas, M. & Rezakazemi, M. A Comprehensive Review on Recent Advances in Two-Dimensional (2D) Hexagonal Boron Nitride. *ACS Appl Electron Mater* **3**, 5165–5187 (2021).

33. Roy, S. *et al.* Structure, Properties and Applications of Two-Dimensional Hexagonal Boron Nitride. *Advanced Materials* **33**, 2101589 (2021).

34. Caldwell, J. D. *et al.* Photonics with hexagonal boron nitride. *Nat Rev Mater* **4**, 552–567 (2019).

35. Carvalho, A. *et al.* Phosphorene: from theory to applications. *Nat Rev Mater* **1**, 16061 (2016).

36. Huang, H., Jiang, B., Zou, X., Zhao, X. & Liao, L. Black phosphorus electronics. *Sci Bull (Beijing)* **64**, 1067–1079 (2019).

37. Xia, F., Wang, H., Hwang, J. C. M., Neto, A. H. C. & Yang, L. Black phosphorus and its isoelectronic materials. *Nature Reviews Physics* **1**, 306–317 (2019).

38. Oughaddou, H. *et al.* Silicene, a promising new 2D material. *Prog Surf Sci* **90**, 46–83 (2015).

39. Masson, L. & Prévot, G. Epitaxial growth and structural properties of silicene and other 2D allotropes of Si. *Nanoscale Adv* **5**, 1574–1599 (2023).

40. Jiang, J., Parto, K., Cao, W. & Banerjee, K. Ultimate Monolithic-3D Integration With 2D Materials: Rationale, Prospects, and Challenges. *IEEE Journal of the Electron Devices Society* **7**, 878–887 (2019).

41. Manzeli, S., Ovchinnikov, D., Pasquier, D., Yazyev, O. V & Kis, A. 2D transition metal dichalcogenides. *Nat Rev Mater* **2**, 17033 (2017).

42. Katiyar, A. K. *et al.* 2D Materials in Flexible Electronics: Recent Advances and Future Prospectives. *Chem Rev* **124**, 318–419 (2024).

43. Sokolikova, M. S. & Mattevi, C. Direct synthesis of metastable phases of 2D transition metal dichalcogenides. *Chem Soc Rev* **49**, 3952–3980 (2020).

44. Chhowalla, M. *et al.* The chemistry of two-dimensional layered transition metal dichalcogenide nanosheets. *Nat Chem* **5**, 263–275 (2013).

45. Huang, H. H. *et al.* Controlling phase transition for single-layer MTe2 (M = Mo and W): modulation of the potential barrier under strain. *Physical Chemistry Chemical Physics* **18**, 4086–4094 (2016).

46. Dickinson, R. G. & Pauling, L. THE CRYSTAL STRUCTURE OF MOLYBDENITE. *J Am Chem Soc* **45**, 1466–1471 (1923).

47. Frindt, R. F. Optical Absorption of a Few Unit-Cell Layers of Mo${\mathrm{S}}_{2}$. *Physical Review* **140**, A536–A539 (1965).

48. Wilson, J. A. & Yoffe, A. D. The transition metal dichalcogenides discussion and interpretation of the observed optical, electrical and structural properties. *Adv Phys* **18**, 193–335 (1969).

49. Whitcher, T. J. *et al.* Unravelling strong electronic interlayer and intralayer correlations in a transition metal dichalcogenide. *Nat Commun* **12**, 6980 (2021).

50. Pasquier, D. & Yazyev, O. V. Crystal field, ligand field, and interorbital effects in two-dimensional transition metal dichalcogenides across the periodic table. *2d Mater* **6**, 025015 (2019).

51. Chen, J. & Warner, J. H. Chapter 6 - Atomic structure of defects in transitional metal dichalcogenides using transmission electron microscopy. in *2D Semiconductor Materials and Devices* (eds. Chi, D., Goh, K. E. J. & Wee, A. T. S.) 167–197 (Elsevier, 2020). doi:https://doi.org/10.1016/B978-0-12-816187-6.00006-6.

52. Kertesz, M. & Hoffmann, R. Octahedral vs. trigonal-prismatic coordination and clustering in transition-metal dichalcogenides. *J Am Chem Soc* **106**, 3453–3460 (1984).

53. Power, P. P. Stable Two-Coordinate, Open-Shell (d1–d9) Transition Metal Complexes. *Chem Rev* **112**, 3482–3507 (2012).

54. Mattheiss, L. F. Band Structures of Transition-Metal-Dichalcogenide Layer Compounds. *Phys Rev B* **8**, 3719–3740 (1973).

55. Jain, A. *et al.* Commentary: The Materials Project: A materials genome approach to accelerating materials innovation. *APL Mater* **1**, 011002 (2013).

56. Stewart, G. R. Low Temperature Specific Heat of Layered Transition Metal Dichalcogenides. *J Supercond Nov Magn* **33**, 213–215 (2020).

57. Chaves, A. *et al.* Bandgap engineering of two-dimensional semiconductor materials. *NPJ 2D Mater Appl* **4**, 29 (2020).

58. Madhukar, A. Structural classification of layered dichalcogenides of group IV B, V B and VI B transition metals. *Solid State Commun* **16**, 383–388 (1975).

59. Komarek, K. & Boller, H. 8 International conference of solid compounds of transition elements Extended abstracts. in *Solid compounds of transition elements* (Austria, 1985).

60. Wikipedia. Space group. https://en.wikipedia.org/w/index.php?title=Space_group&oldid=1214698150.

61. Souvignier, B., Wondratschek, H., Aroyo, M. I., Chapuis, G. & Glazer, A. M. Space groups and their descriptions. in *International Tables for Crystallography, Online MRW* 42–74 (2016). doi:https://doi.org/10.1107/97809553602060000922.

62. Koster, G. F. Space Groups and Their Representations. in *Solid State Physics* (eds. SEITZ, F. & TURNBULL, D.) vol. 5 173–256 (Academic Press, 1957).

63. Arribas, V., Casas, L., Estop, E. & Labrador, M. Interactive PDF files with embedded 3D designs as support material to study the 32 crystallographic point groups. *Comput Geosci* **62**, 53–61 (2014).

64. Structure of Materials. An Introduction to Crystallography, Diffraction and Symmetry. By Marc De Graef.

65. Zhou, Y. *et al.* Pressure-induced Td to 1T′ structural phase transition in WTe2. *AIP Adv* **6**, 075008 (2016).

66. Bastos, C. M. O., Besse, R., Da Silva, J. L. F. & Sipahi, G. M. Ab initio investigation of structural stability and exfoliation energies in transition metal dichalcogenides based on Ti-, V-, and Mo-group elements. *Phys Rev Mater* **3**, 44002 (2019).

67. Wang, C. *et al.* Type-II Ising Superconductivity in Two-Dimensional Materials with Spin-Orbit Coupling. *Phys Rev Lett* **123**, 126402 (2019).

68. Wickramaratne, D. & Mazin, I. I. Ising superconductivity: A first-principles perspective. *Appl Phys Lett* **122**, 240503 (2023).

69. Bandaru, N. R. Structure and Optical properties of Transition Metal Dichalcogenides (TMDs) – MX2 (M = Mo, W & X = S, Se) under High Pressure and High Temperature conditions. *UNLV Theses, Dissertations, Professional Papers, and Capstones* (2015) doi:10.34917/7777293.

70. Xu, M. *et al.* A hidden symmetry-broken phase of MoS2 revealed as a superior photovoltaic material. *J Mater Chem A Mater* **6**, 16087–16093 (2018).

71. Tsai, J.-Y., Pan, J., Lin, H., Bansil, A. & Yan, Q. Antisite defect qubits in monolayer transition metal dichalcogenides. *Nat Commun* **13**, 492 (2022).

72. W G Dawson & D W Bullett. Electronic structure and crystallography of MoTe2 and WTe2. *Journal of Physics C: Solid State Physics* **20**, 6159 (1987).

73. Fleischauer, P. D., Lince, J. R., Bertrand, P. A. & Bauer, R. Electronic structure and lubrication properties of molybdenum disulfide: a qualitative molecular orbital approach. *Langmuir* **5**, 1009–1015 (1989).

74. Fleischauer, P. D., Lince, J. R., Bertrand, P. A. & Bauer, R. Electronic structure and lubrication properties of molybdenum disulfide: a qualitative molecular orbital approach. *Langmuir* **5**, 1009–1015 (1989).

75. Wilson, J. A. & Yoffe, A. D. The transition metal dichalcogenides discussion and interpretation of the observed optical, electrical and structural properties. *Adv Phys* **18**, 193–335 (1969).

76. Kim, J. H., Sung, H. & Lee, G.-H. Phase Engineering of Two-Dimensional Transition Metal Dichalcogenides. *Small Science* **4**, 2300093 (2024).

77. Kim, J. H., Sung, H. & Lee, G.-H. Phase Engineering of Two-Dimensional Transition Metal Dichalcogenides. *Small Science* **4**, 2300093 (2024).

78. Chen, S.-Y., Goldstein, T., Venkataraman, D., Ramasubramaniam, A. & Yan, J. Activation of New Raman Modes by Inversion Symmetry Breaking in Type II Weyl Semimetal Candidate T′-MoTe2. *Nano Lett* **16**, 5852–5860 (2016).

79. Qiao, J. *et al.* Ultrasensitive Near-Infrared MoTe2 Photodetectors with Monolithically Integrated Fresnel Zone Plate Metalens. *Adv Opt Mater* **10**, 2200375 (2022).

80. Zhao, Y. *et al.* Electronic and Near-Infrared-II Optical Properties of I-Doped Monolayer MoTe2: A First-Principles Study. *ACS Omega* **7**, 11956–11963 (2022).

81. Razeghi, M. *Fundamentals of Solid State Engineering*. (Springer Publishing Company, Incorporated, 2009).

82. Misra, P. K. Chapter 4 - Nearly Free Electron Model. in *Physics of Condensed Matter* (ed. Misra, P. K.) 95–130 (Academic Press, Boston, 2012). doi:https://doi.org/10.1016/B978-0-12-384954-0.00004-9.

83. Ramzan, M. S. & Cocchi, C. Strained Monolayer MoTe[sub.2] as a Photon Absorber in the Telecom Range. *Nanomaterials* **13**, NA (2023).

84. Chaves, A. *et al.* Bandgap engineering of two-dimensional semiconductor materials. *NPJ 2D Mater Appl* **4**, 29 (2020).

85. Enyashin, A. N. & Seifert, G. Electronic properties of MOS 2 monolayer and related structures. in (2014).

86. Cai, X. *et al.* Bridging the gap between atomically thin semiconductors and metal leads. *Nat Commun* **13**, 1777 (2022).

87. Samadi, M. *et al.* Group 6 transition metal dichalcogenide nanomaterials: synthesis, applications and future perspectives. *Nanoscale Horiz.* **3**, 90–204 (2018).

88. Ali, L. *et al.* Exfoliation of MoS2 Quantum Dots: Recent Progress and Challenges. *Nanomaterials* **12**, (2022).

89. Koster, G. F. Space Groups and Their Representations. in *Solid State Physics* (eds. SEITZ, F. & TURNBULL, D.) vol. 5 173–256 (Academic Press, 1957).

90. Joensen, P., Frindt, R. F. & Morrison, S. R. Single-layer MoS2. *Mater Res Bull* **21**, 457–461 (1986).

91. Kopaczek, J. *et al.* Direct optical transitions at K- and H-point of Brillouin zone in bulk MoS2, MoSe2, WS2, and WSe2. *J Appl Phys* **119**, 235705 (2016).

92. Liu, G.-B., Xiao, D., Yao, Y., Xu, X. & Yao, W. Electronic structures and theoretical modelling of two-dimensional group-VIB transition metal dichalcogenides. *Chem. Soc. Rev.* **44**, 2643–2663 (2015).

93. Krowne, C. M. Chapter Two - Determination of reciprocal lattice from direct space in 3D and 2D – Examination of hexagonal band structure. in *Advances in Imaging and Electron Physics* (eds. Hawkes, P. W. & Hÿtch, M.) vol. 210 7–22 (Elsevier, 2019).

94. Structure change, layer sliding, and metallization in high-pressure MoS2.

95. Pandey, S. K., Das, R. & Mahadevan, P. Layer-Dependent Electronic Structure Changes in Transition Metal Dichalcogenides: The Microscopic Origin. *ACS Omega* **5**, 15169–15176 (2020).

96. Peng, Z., Chen, X., Fan, Y., Srolovitz, D. J. & Lei, D. Strain engineering of 2D semiconductors and graphene: from strain fields to band-structure tuning and photonic applications. *Light Sci Appl* **9**, 190 (2020).

97. Paul, S., Talukdar, S., Singh, R. S. & Saha, S. Topological Phase Transition in MoTe2: A Review. *physica status solidi (RRL) – Rapid Research Letters* **17**, 2200420 (2023).

98. Zhuang, W., Chen, Z. & Wang, X. Large-area fabrication of 2D layered topological semimetal films and emerging applications. *Adv Phys X* **7**, 2034529 (2022).

99. Band structure of MoS2 , MoSe2, and a-MoTe2- Angle-resolved photoelectron spectroscopy and ab initio calculations.

100. Colloquium- Excitons in atomically thin transition metal dichalcogenides.

101. Silva-Guillén, J. Á., San-Jose, P. & Roldán, R. Electronic Band Structure of Transition Metal Dichalcogenides from Ab Initio and Slater–Koster Tight-Binding Model. *Applied Sciences* **6**, (2016).

102. Dufferwiel, S. *et al.* Valley coherent exciton-polaritons in a monolayer semiconductor. *Nat Commun* **9**, 4797 (2018).

103. Kormányos, A. *et al.* k·p theory for two-dimensional transition metal dichalcogenide semiconductors. *2d Mater* **2**, 022001 (2015).

104. Zhang, X. *et al.* Phonon and Raman scattering of two-dimensional transition metal dichalcogenides from monolayer, multilayer to bulk material. *Chem. Soc. Rev.* **44**, 2757–2785 (2015).

105. Tan, Q.-H. *et al.* Breakdown of Raman selection rules by Fröhlich interaction in few-layer WS2. *Nano Res* **14**, 239–244 (2021).

106. Voiry, D., Mohite, A. & Chhowalla, M. Phase engineering of transition metal dichalcogenides. *Chem Soc Rev* **44**, 2702–2712 (2015).

107. Park, S. *et al.* Phase Engineering of Transition Metal Dichalcogenides with Unprecedentedly High Phase Purity, Stability, and Scalability via Molten-Metal-Assisted Intercalation. *Advanced Materials* **32**, 2001889 (2020).

108. Fraser, J. P. *et al.* Selective phase growth and precise-layer control in MoTe2. *Commun Mater* **1**, 48 (2020).

109. Wang, Y. *et al.* Structural phase transition in monolayer MoTe2 driven by electrostatic doping. *Nature* **550**, 487–491 (2017).

110. Zhou, Y. *et al.* Pressure-induced Td to 1T′ structural phase transition in WTe2. *AIP Adv* **6**, 075008 (2016).

111. Chen, J. *et al.* Quantum Effects and Phase Tuning in Epitaxial Hexagonal and Monoclinic MoTe2 Monolayers. *ACS Nano* **11**, 3282–3288 (2017).

112. Sun, L. *et al.* An Investigation in Phase Transition of MoTe2 Film with Continuous Tellurization Reaction. *IOP Conf Ser Mater Sci Eng* **677**, 022123 (2019).

113. Huang, J.-H. *et al.* Polymorphism Control of Layered MoTe2 through Two-Dimensional Solid-Phase Crystallization. *Sci Rep* **9**, 8810 (2019).

114. Castellanos-Gomez, A., Agraït, N. & Rubio-Bollinger, G. Optical identification of atomically thin dichalcogenide crystals. *Appl Phys Lett* **96**, 213116 (2010).

115. Novoselov, K. S. *et al.* Two-dimensional atomic crystals. *Proceedings of the National Academy of Sciences* **102**, 10451–10453 (2005).

116. Velický, M. *et al.* Mechanism of Gold-Assisted Exfoliation of Centimeter-Sized Transition-Metal Dichalcogenide Monolayers. *ACS Nano* **12**, 10463–10472 (2018).

117. Li, Y., Kuang, G., Jiao, Z., Yao, L. & Duan, R. Recent progress on the mechanical exfoliation of 2D transition metal dichalcogenides. *Mater Res Express* **9**, 122001 (2022).

118. Kang, K., Chen, S., Fu, S. & Yang, E.-H. Synthesis of Transition Metal Dichalcogenides (TMDs). in *Progress in Nanoscale and Low-Dimensional Materials and Devices: Properties, Synthesis, Characterization, Modelling and*

Applications (eds. Ünlü, H. & Horing, N. J. M.) 155–179 (Springer International Publishing, Cham, 2022). doi:10.1007/978-3-030-93460-6_4.

119. Cantarella, M. *et al.* Mechanical milling: a sustainable route to induce structural transformations in MoS2 for applications in the treatment of contaminated water. *Sci Rep* **9**, 974 (2019).

120. Pazhamalai, P., Krishnamoorthy, K., Manoharan, S. & Kim, S.-J. High energy symmetric supercapacitor based on mechanically delaminated few-layered MoS2 sheets in organic electrolyte. *J Alloys Compd* **771**, 803–809 (2019).

121. Yang, R. *et al.* High-yield production of mono- or few-layer transition metal dichalcogenide nanosheets by an electrochemical lithium ion intercalation-based exfoliation method. *Nat Protoc* **17**, 358–377 (2022).

122. Eames, C. & Islam, M. S. Ion Intercalation into Two-Dimensional Transition-Metal Carbides: Global Screening for New High-Capacity Battery Materials. *J Am Chem Soc* **136**, 16270–16276 (2014).

123. An, S.-J., Kim, Y. H., Lee, C., Park, D. Y. & Jeong, M. S. Exfoliation of Transition Metal Dichalcogenides by a High-Power Femtosecond Laser. *Sci Rep* **8**, 12957 (2018).

124. Tummala, P. P. *et al.* Large Area Growth and Phase Selectivity of MoTe2 Nanosheets through Simulation-Guided CVD Tellurization. *Adv Mater Interfaces* **10**, 2200971 (2023).

125. Shidpour, R., Vosoughi, M., Maghsoudi, H. & Simchi, A. A general two-step chemical vapor deposition procedure to synthesize highly crystalline transition metal dichalcogenides: A case study of MoS2. *Mater Res Bull* **76**, 473–478 (2016).

126. Kang, T. *et al.* Strategies for Controlled Growth of Transition Metal Dichalcogenides by Chemical Vapor Deposition for Integrated Electronics. *ACS Materials Au* **2**, 665–685 (2022).

127. Kang, K., Chen, S. & Yang, E.-H. 12 - Synthesis of transition metal dichalcogenides. in *Synthesis, Modeling, and Characterization of 2D Materials, and Their Heterostructures* (eds. Yang, E.-H., Datta, D., Ding, J. & Hader, G.) 247–264 (Elsevier, 2020). doi:https://doi.org/10.1016/B978-0-12-818475-2.00012-X.

128. Cai, J., Han, X., Wang, X. & Meng, X. Atomic Layer Deposition of Two-Dimensional Layered Materials: Processes, Growth Mechanisms, and Characteristics. *Matter* **2**, 587–630 (2020).

129. Juvaid, M. M. & Ramachandra Rao, M. S. Wafer scale growth of MoS2 and WS2 by pulsed laser deposition. *Mater Today Proc* **35**, 494–496 (2021).

130. Muratore, C., Voevodin, A. A. & Glavin, N. R. Physical vapor deposition of 2D Van der Waals materials: a review. *Thin Solid Films* **688**, 137500 (2019).

131. Vishwanath, S. *et al.* MBE growth of few-layer 2H-MoTe2 on 3D substrates. *J Cryst Growth* **482**, 61–69 (2018).

132. Walsh, L. A., Addou, R., Wallace, R. M. & Hinkle, C. L. Chapter 22 - Molecular Beam Epitaxy of Transition Metal Dichalcogenides. in *Molecular Beam Epitaxy (Second Edition)* (ed. Henini, M.) 515–531 (Elsevier, 2018). doi:https://doi.org/10.1016/B978-0-12-812136-8.00024-4.

133. Gaspari, F. 2.4 Thin Films. in *Comprehensive Energy Systems* (ed. Dincer, I.) 88–116 (Elsevier, Oxford, 2018). doi:https://doi.org/10.1016/B978-0-12-809597-3.00214-5.

134. Huang, J.-H. *et al.* Large-area few-layer MoS2 deposited by sputtering. *Mater Res Express* **3**, 065007 (2016).

135. Hatayama, S. *et al.* Phase control of sputter-grown large-area MoTe2 films by preferential sublimation of Te: amorphous, 1T′ and 2H phases. *J. Mater. Chem. C* **10**, 10627–10635 (2022).

136. Almeida, K. *et al.* High-Vacuum Particulate-Free Deposition of Wafer-Scale Mono-, Bi-, and Trilayer Molybdenum Disulfide with Superior Transport Properties. *ACS Appl Mater Interfaces* **10**, 33457–33463 (2018).

137. Bernath, P. F. & Knee, J. L. Spectra of Atoms and Molecules. *Am J Phys* **64**, 93–94 (1996).

138. Watts, J. F. Encyclopedia of materials characterization: C. Richard Brundle, Charles A. Evans Jr and Shaun Wilson (Eds) Butterworth-Heinemann, Stoneham, USA, 1992, ISBN 0-7506-9168-9, 750pp. £75. *Mater Des* **14**, (1993).

139. Larkin, P. Chapter 4 - Environmental Dependence of Vibrational Spectra. in *Infrared and Raman Spectroscopy* (ed. Larkin, P.) 55–62 (Elsevier, Oxford, 2011). doi:https://doi.org/10.1016/B978-0-12-386984-5.10004-7.

140. Larkin, P. Chapter 5 - Origin of Group Frequencies. in *Infrared and Raman Spectroscopy* (ed. Larkin, P.) 63–72 (Elsevier, Oxford, 2011). doi:https://doi.org/10.1016/B978-0-12-386984-5.10005-9.

141. Larkin, P. Chapter 6 - IR and Raman Spectra-Structure Correlations: Characteristic Group Frequencies. in *Infrared and Raman Spectroscopy* (ed. Larkin, P.) 73–115 (Elsevier, Oxford, 2011). doi:https://doi.org/10.1016/B978-0-12-386984-5.10006-0.

142. Instrumentation in Raman spectroscopy- elementary theory and practice.

143. Emmanuel, N., Nair, R. B., Abraham, B. & Yoosaf, K. Fabricating a Low-Cost Raman Spectrometer to Introduce Students to Spectroscopy Basics and Applied Instrument Design. *J Chem Educ* **98**, 2109–2116 (2021).

144. Jones, R. R., Hooper, D. C., Zhang, L., Wolverson, D. & Valev, V. K. Raman Techniques: Fundamentals and Frontiers. *Nanoscale Res Lett* **14**, 231 (2019).

145. An introduction to spectroscopic methods Geiger.

146. Iqbal, M. W., Shahzad, K., Akbar, R. & Hussain, G. A review on Raman finger prints of doping and strain effect in TMDCs. *Microelectron Eng* **219**, 111152 (2020).

147. Raman Instrumentation.

148. McCreary, K. M., Hanbicki, A. T., Sivaram, S. V & Jonker, B. T. A- and B-exciton photoluminescence intensity ratio as a measure of sample quality for transition metal dichalcogenide monolayers. *APL Mater* **6**, 111106 (2018).

149. PL Libre.

150. Kumar, C. S. S. R. UV-VIS and Photoluminescence Spectroscopy for Nanomaterials Characterization. in (2013).

151. Tebyetekerwa, M. *et al.* Mechanisms and Applications of Steady-State Photoluminescence Spectroscopy in Two-Dimensional Transition-Metal Dichalcogenides. *ACS Nano* **14**, 14579–14604 (2020).

152. Pavić, I., Šoda, J., Gašparić, V. & Ivanda, M. Raman and Photoluminescence Spectroscopy with a Variable Spectral Resolution. *Sensors* **21**, (2021).

153. Nolot, E. *et al.* In-line characterization of ultrathin transition metal dichalcogenides using X-ray fluorescence and X-ray photoelectron spectroscopy. *Spectrochim Acta Part B At Spectrosc* **166**, 105788 (2020).

154. Stevie, F. A. & Donley, C. L. Introduction to x-ray photoelectron spectroscopy. *Journal of Vacuum Science & Technology A* **38**, 063204 (2020).

155. Williams, D. B. & Carter, C. B. Transmission Electron Microscopy: A Textbook for Materials Science. in (1996).

156. Ayache, J., Beaunier, L., Boumendil, J., Ehret, G. & Laub, D. Techniques: General Introduction. in *Sample Preparation Handbook for Transmission Electron Microscopy: Techniques* (eds. Ayache, J., Beaunier, L., Boumendil, J., Ehret, G. & Laub, D.) 1–4 (Springer New York, New York, NY, 2010). doi:10.1007/978-1-4419-5975-1_1.

157. Fahlman, B. D. Materials Characterization. in *Materials Chemistry* (ed. Fahlman, B. D.) 721–829 (Springer International Publishing, Cham, 2023). doi:10.1007/978-3-031-18784-1_7.

158. Isaacson, M., Ohtsuki, M. & Utlaut, M. Electron Microscopy of Individual Atoms. in *Introduction to Analytical Electron Microscopy* (eds. Hren, J. J., Goldstein, J. I. & Joy, D. C.) 343–368 (Springer US, Boston, MA, 1979). doi:10.1007/978-1-4757-5581-7_13.

159. Schleberger, M., Speller, S. & Heiland, W. 6. Surface Characterization. *Experimental Methods in The Physical Sciences* **30**, 291–331 (1997).

160. Surface Structure Determination by LEED and X-rays. in *Surface Structure Determination by LEED and X-rays* (eds. Moritz, W. & Van Hove, M. A.) iii–iii (Cambridge University Press, Cambridge, 2022).

161. Hoffer, S. Low energy electron diffraction (LEED) and sum frequency generation (SFG) vibrational spectroscopy studies of solid-vacuum, solid-air and solid-liquid interfaces. (United States, 2002). doi:10.2172/803862.

162. Roberts, J. G. Surface structure determinations of crystalline ionic thin films grown on transition metal single crystal surfaces by low energy electron diffraction. (United States, 2000). doi:10.2172/764397.

163. Glazer, A. M. *A Journey into Reciprocal Space*. (Morgan & Claypool Publishers, 2017). doi:10.1088/978-1-6817-4621-0.

164. Airaksinen, V.-M. Chapter 15 - Silicon Wafer and Thin Film Measurements. in *Handbook of Silicon Based MEMS Materials and Technologies (Second Edition)* (eds. Tilli, M. et al.) 381–390 (William Andrew Publishing, Boston, 2015). doi:https://doi.org/10.1016/B978-0-323-29965-7.00015-4.

165. Resistivity. in *Semiconductor Material and Device Characterization* 1–59 (John Wiley & Sons, Ltd, 2005). doi:https://doi.org/10.1002/0471749095.ch1.

166. Fauzi, F., Rianjanu, A., Santoso, I. & Triyana, K. Gas and humidity sensing with quartz crystal microbalance (QCM) coated with graphene-based materials – A mini review. *Sens Actuators A Phys* **330**, 112837 (2021).

167. Empante, T. A. *et al.* Chemical Vapor Deposition Growth of Few-Layer MoTe2 in the 2H, 1T′, and 1T Phases: Tunable Properties of MoTe2 Films. *ACS Nano* **11**, 900–905 (2017).

168. Keum, D. H. *et al.* Bandgap opening in few-layered monoclinic MoTe2. *Nat Phys* **11**, 482–486 (2015).

169. Ohtake, A., Yang, X. & Nara, J. Structure and morphology of 2H-MoTe2 monolayer on GaAs(111)B grown by molecular-beam epitaxy. *NPJ 2D Mater Appl* **6**, 35 (2022).

170. Huang, J.-H. *et al.* Large-Area 2D Layered MoTe2 by Physical Vapor Deposition and Solid-Phase Crystallization in a Tellurium-Free Atmosphere. *Adv Mater Interfaces* **4**, 1700157 (2017).

171. Roy, A. *et al.* Structural and Electrical Properties of MoTe2 and MoSe2 Grown by Molecular Beam Epitaxy. *ACS Appl Mater Interfaces* **8**, 7396–7402 (2016).

172. Wu, D. *et al.* Phase-controlled van der Waals growth of wafer-scale 2D MoTe2 layers for integrated high-sensitivity broadband infrared photodetection. *Light Sci Appl* **12**, 5 (2023).

173. Thakar, K. & Lodha, S. Optoelectronic and photonic devices based on transition metal dichalcogenides. *Mater Res Express* **7**, 014002 (2020).

174. W G Dawson & D W Bullett. Electronic structure and crystallography of MoTe2 and WTe2. *Journal of Physics C: Solid State Physics* **20**, 6159 (1987).

175. Pace, S. *et al.* Synthesis of Large-Scale Monolayer 1T′-MoTe2and Its Stabilization via Scalable hBN Encapsulation. *ACS Nano* **15**, 4213–4225 (2021).

176. Guo, J. & Liu, K. Recent Progress in Two-Dimensional MoTe2 Hetero-Phase Homojunctions. *Nanomaterials* vol. 12 Preprint at https://doi.org/10.3390/nano12010110 (2022).

177. Sun, L. *et al.* An Investigation in Phase Transition of MoTe2 Film with Continuous Tellurization Reaction. in *IOP Conference Series: Materials Science and Engineering* vol. 677 (IOP Publishing Ltd, 2019).

178. Lezama, I. G. *et al.* Indirect-to-Direct Band Gap Crossover in Few-Layer MoTe2. *Nano Lett* **15**, 2336–2342 (2015).

179. Gong, C. *et al.* Band alignment of two-dimensional transition metal dichalcogenides: Application in tunnel field effect transistors. *Appl Phys Lett* **103**, 053513 (2013).

180. Yu, W. *et al.* High-Yield Exfoliation of Monolayer 1T'-MoTe2 as Saturable Absorber for Ultrafast Photonics. *ACS Nano* **15**, 18448–18457 (2021).

181. Diaz, H. C., Chaghi, R., Ma, Y. & Batzill, M. Molecular beam epitaxy of the van der Waals heterostructure MoTe2 on MoS2: phase, thermal, and chemical stability. *2d Mater* **2**, 044010 (2015).

182. Hynek, D. J. *et al.* cm2-Scale Synthesis of MoTe2 Thin Films with Large Grains and Layer Control. *ACS Nano* **15**, 410–418 (2021).

183. Yang, L. *et al.* Ultrahigh yield and large-scale fast growth of large-size high-quality van der Waals transition-metal telluride single crystals. *Cell Rep Phys Sci* **3**, 100953 (2022).

184. Tao, L., Zhou, Y. & Xu, J.-B. Phase-controlled epitaxial growth of MoTe2: Approaching high-quality 2D materials for electronic devices with low contact resistance. *J Appl Phys* **131**, 110902 (2022).

185. Naylor, C. H. *et al.* Monolayer Single-Crystal 1T′-MoTe2 Grown by Chemical Vapor Deposition Exhibits Weak Antilocalization Effect. *Nano Lett* **16**, 4297–4304 (2016).

186. Huang, Y. *et al.* Universal mechanical exfoliation of large-area 2D crystals. *Nat Commun* **11**, 2453 (2020).

187. Jeong, J. *et al.* Positive charge-mediated phase modulation of MoTe2 synthesized by molecular beam epitaxy. *Appl Surf Sci* **623**, 156988 (2023).

188. Yuan, S. *et al.* Room-temperature ferroelectricity in MoTe2 down to the atomic monolayer limit. *Nat Commun* **10**, 1775 (2019).

189. He, Q. *et al.* Molecular Beam Epitaxy Scalable Growth of Wafer-Scale Continuous Semiconducting Monolayer MoTe2 on Inert Amorphous Dielectrics. *Advanced Materials* **31**, 1901578 (2019).

190. Tang, S. *et al.* Electronic structure of monolayer 1T′-MoTe2 grown by molecular beam epitaxy. *APL Mater* **6**, 026601 (2017).

191. Almeida, K. *et al.* High-Vacuum Particulate-Free Deposition of Wafer-Scale Mono-, Bi-, and Trilayer Molybdenum Disulfide with Superior Transport Properties. *ACS Appl Mater Interfaces* **10**, 33457–33463 (2018).

192. Kumar, R. *et al.* Growth of 2D MoS2 and MoSe2 layers for photodetector application. *Mater Today Proc* (2023) doi:https://doi.org/10.1016/j.matpr.2023.04.407.

193. Jiao, L. *et al.* Molecular-beam epitaxy of monolayer MoSe2: growth characteristics and domain boundary formation. *New J Phys* **17**, 053023 (2015).